Journal of Computational Physics – 5029

JOURNAL OF COMPUTATIONAL PHYSICS 116, 3–25 (1995)

Nonlinear Oscillations of Two-Dimensional, Rotating Inviscid Drops*

T. W. PATZEK†

Department of Materials Science and Mineral Engineering, University of California, Berkeley, California 94720

O. A. BASARAN

Oak Ridge National Laboratory, Chemical Technology Division, Oak Ridge, Tennessee 37831

R. E. BENNER

Sandia National Laboratories, Albuquerque, New Mexico 87185

AND

L. E. SCRIVEN

Department of Chemical Engineering and Materials Science, University of Minnesota, Minneapolis, Minnesota 55455

Received March 15, 1993; revised February 15, 1994

We examine the nonlinear response of a drop, rotating as a rigid body at fixed angular velocity, to two-dimensional finite-amplitude disturbances. With these restrictions, the liquid velocity becomes a superposition of the solid-body rotation and the gradient of a velocity potential. To find the drop motion, we solve an *integro-differential* Bernoulli's equation for the drop shape and Laplace's equation for the velocity potential field within the drop. The integral part of Bernoulli's equation couples all parts of the drop's surface and sets this problem apart from that of the oscillations of nonrotating drops. We use Galerkin's weighted residual method with finite element basis functions which are deployed on a mesh that deforms in proportion to the deformation of the free surface. To alleviate the roundoff error in the initial conditions of the drop motion, we use a Fourier filter which turns off as soon as the highest resolved oscillation mode grows above the machine noise level. The results include sequences of drop shapes, Fourier analysis of oscillation frequencies, and evolution in time of the components of total mechanical energy of the drop. The Fourier power spectral analysis of large-amplitude oscillations of the drop reveals frequency shifts similar to those of the nonrotating free drops. Constant drop volume, total energy, and angular momentum as well as vanishing mass flow across the drop surface are the standards of accuracy against which we test the nonlinear motion of the drop over tens or *hundreds* of oscillation periods. Finally, we demonstrate that our finite element method has superior stability, accuracy, and computational efficiency *over several boundary element algorithms that have previously* appeared in the literature.

* Research sponsored by the University of California at Berkeley; the Division of Chemical Sciences, Office of Basic Energy Sciences, U.S. DOE under Contract DE-AC05-84OR21400 with Martin Marietta Energy Systems; and NASA Fund for Independent Research. R. E. Benner was partially supported by a Dissertation Fellowship from the University of Minnesota.

† Author to whom correspondence should be addressed.

1. INTRODUCTION

An infinite column of inviscid liquid at rest, held together by the action of surface tension, has been used to model liquid jet breakup ever since Savart [32] and Plateau [27] observed and Rayleigh [29] proved that such a column is unstable to infinitesimal axisymmetric disturbances whose wavelength in the axial direction is greater than the circumference of the cross section. This instability is caused by a decrease of the surface area of the column and the continuous diversion of the excess surface energy to kinetic energy of the growing disturbance. Rayleigh [30] also found that the liquid column, whether inviscid or viscous, is always stable to two-dimensional planar or translationally symmetric perturbations that distort its cross section to a noncircular shape. Thus, if the axisymmetric mode of instability is suppressed, the liquid column is stable and becomes an oft-used *prototype* of fully three-dimensional drops. For example, a rotating captive drop [11] stabilized *against the Rayleigh instability by an axially symmetric* electrical field [12] can be approximated by the cylindrical column.

Hocking and Michael [14] and Hocking [15] added

0021-9991/95 $6.00

rotation to Rayleigh's analyses and examined the linear stability of a gyrostatically rotating liquid column to planar inviscid and viscous disturbances. The linear response of an oscillating, two-dimensional liquid column rotating at fixed angular velocity is governed by two waves that may become coupled, depending on the velocity of rotation. Hocking and Michael [14] showed that this column remains stable to planar disturbances provided that the angular velocity of rotation remains below a threshold value that marks the first of a sequence of marginal stability points. At the first point, the column becomes marginally stable to a two-lobed perturbation; at the (n-1)*th* point, it becomes marginally stable to an n-lobed perturbation. Hocking and Michael did not investigate the families that bifurcate or branch from the family of perfect cylinders at the onset of instability; such nonlinear bifurcating families were only recently calculated [6].

In the last decade, interest in the study of rotating, oscillating drops has been revived by the need to (1) guide and support fundamental experiments with such drops that are either free in space or levitated on earth [1, 31, 37], and (2) advance methods of containerless material processing in ultralow gravity [8]. Motivated by recent experiments with rotating drops, Busse [7] developed a linear theory of oscillations of nearly spherical, rotating drops. However, theoretical analysis of *finite* amplitude oscillations of rotating drops has not received any attention to date and is the goal of this paper.

Here we consider the finite amplitude oscillations of a rotating two-dimensional drop of inviscid incompressible liquid held together by surface tension (Fig. 1). In inviscid incompressible flow, the material derivative of the vorticity [3] in an *inertial* frame of reference is given by

$$\frac{D\boldsymbol{\omega}}{Dt} = \boldsymbol{\omega} \cdot \nabla \mathbf{v}. \tag{1}$$

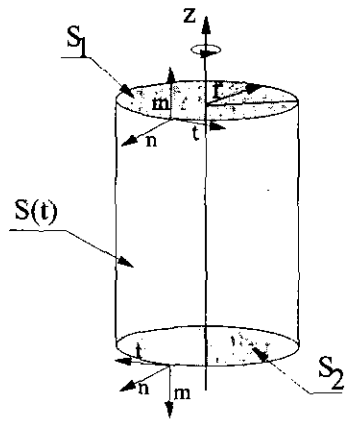

FIG. 1. Translationally symmetric rotating drop; unit length section liquid column.

Here $\mathbf{v}$ is the velocity, $\boldsymbol{\omega} = \nabla \times \mathbf{v}$ is the vorticity, and t is time. If, in addition, the oscillations are confined to cross-sectional planes of the cylinder and are the same in all such planes, i.e., translationally symmetric, then $\boldsymbol{\omega} \perp \nabla \mathbf{v}$ and

$$\frac{D\boldsymbol{\omega}}{Dt} = \mathbf{0}; \tag{2}$$

i.e., the vorticity of fluid particles is time-invariant. This can be explained as follows. When the unperturbed cylinder is forced to rotate as a rigid body, both the angular velocity of rotation and the vorticity are constant and uniform. Translationally symmetric oscillations of such a cylinder can only shift the vortex lines and, therefore, the vorticity must remain constant and uniform: the cylinder motion is irrotational *relative* to the solid body rotation.

In Section 2 we present the nonlinear equations that govern the finite-amplitude oscillations of the two-dimensional rotating drop and the boundary and initial conditions used in the calculations. We show that when the drop rotates, the balance of momentum at the drop/ambient fluid interface becomes an integro-differential Bernoulli equation. In Section 3 we present an implicit method of integrating the equations governing drop motion in time and introduce a Fourier filter to control and alleviate roundoff error. In Section 4 we discuss the results and compare the present method with published boundary element algorithms. In addition, in Appendix A, we prove that the oscillations of the two-dimensional rotating drop conserve total mechanical energy and angular momentum. The governing equations are transformed into their weak or Galerkin form in Appendix B.

2. EQUATIONS OF DROP MOTION

Motion of a column of incompressible, inviscid liquid, immersed in tenuous gas that exerts uniform pressure and negligible viscous drag on the column, conserves mass and linear momentum at all times, provided that the center of mass of the column is not accelerated, and neither the liquid evaporates nor the gas condenses. Thus, in a stationary frame of reference,

$$\nabla \cdot \mathbf{v} = 0 \qquad \text{in } V, \tag{3}$$

and

$$\frac{\partial \mathbf{v}}{\partial t} - \mathbf{v} \times \boldsymbol{\omega} = -\nabla\left(\frac{p}{\rho} + \frac{1}{2} v^2\right) \qquad \text{in } V. \tag{4}$$

Here V is the drop volume, p the pressure, and ρ the density

of the liquid. At the drop surface $S(t)$, Eqs. (3)–(4) are subject to the kinematic condition

$$\mathbf{n}\cdot(\mathbf{v}-\mathbf{v}_S)=0 \qquad \text{on } S(t), \tag{5}$$

and the normal stress balance

$$p(\mathbf{x},t)=-2H\sigma \qquad \text{on } S(t). \tag{6}$$

These conditions express the principles of mass and momentum conservation at the drop surface, where the velocity is $\mathbf{v}_S$; the surface tension is σ; and the local mean curvature H is given by the surface divergence ∇_S of the outward unit normal $\mathbf{n}$ [38],

$$H(\mathbf{x},t)=-\tfrac{1}{2}\nabla_S\cdot\mathbf{n}. \tag{7}$$

The constant and uniform pressure outside the drop is set to zero.

The motions considered here are irrotational relative to the solid-body rotation of the unperturbed drop. Thus, we assume that the velocity $\mathbf{v}$ in Eqs. (3)–(5) is the sum of the solid-body rotation at a *fixed* angular velocity Ω and a gradient of velocity potential $\phi(\mathbf{x},t)$ that represents a finite, translationally symmetric velocity disturbance:

$$\mathbf{v}=\Omega r\mathbf{e}_\theta+\nabla\phi \qquad \text{in } V. \tag{8}$$

Here r is the radial distance from the rotation axis. In Eq. (8) and below $(\mathbf{e}_r,\mathbf{e}_\theta,\mathbf{e}_z)$ are the radial, azimuthal and axial unit vectors of the cylindrical polar coordinate system (r,θ,z) centered on the axis of rotation.

Equations (3) and (8) combine into Laplace's equation for velocity potential:

$$\nabla^2\phi=0 \qquad \text{in } V. \tag{9}$$

The translationally symmetric cylindrical drop

$$V\equiv\{(r,\theta): r\in[0,f(\theta,t)],\ \theta\in[0,2\pi]\}\times z, \tag{10}$$

is bounded by a free surface $S(t)$ represented in the cylindrical polar coordinates as

$$\mathbf{r}=f(\theta,t)\,\mathbf{e}_r+z\mathbf{e}_z, \tag{11}$$

where $f(\theta,t)$ is the interface shape function. Because of translational symmetry, the problem is two-dimensional and does not depend on z. The otherwise redundant z-coordinate is kept only for dimensional consistency. The representation (11) is convenient, but it fails for certain extreme deformations of the drop by becoming multiple-valued.

Equations (4) and (8) yield [14]

$$\nabla B=2\Omega\nabla\times(\phi\mathbf{e}_z)=-2\Omega\mathbf{e}_z\times\nabla\phi \qquad \text{in } V, \tag{12}$$

where

$$B\equiv\frac{p}{\rho}+\frac{\partial\phi}{\partial t}+\frac{1}{2}(\nabla\phi)^2-\frac{1}{2}(\Omega r)^2+\Omega\frac{\partial\phi}{\partial\theta} \qquad \text{in } V. \tag{13}$$

The quantity B satisfies Laplace's equation within the drop volume

$$\nabla^2 B=0 \qquad \text{in } V. \tag{14}$$

In the absence of rotation, $\Omega=0$, and Eq. (12) can be readily integrated to $B=0$ (the integration constant can be set to zero without loss of generality, cf. [20]). When $\Omega\neq 0$, Eq. (12) is nonlinear: it can either be (i) linearized and solved analytically for infinitesimal amplitude perturbations from the cylindrical column shape [14], or (ii) it can be integrated numerically, as in this paper, for finite amplitude departures. Integration of Eq. (12) along the drop/ambient fluid interface in the (r,θ) plane gives

$$\begin{aligned}B(s,t)-B(0,t)&=\int_0^s\nabla B\cdot\mathbf{t}\,ds'=-2\Omega\int_0^s(\mathbf{e}_z\times\nabla\phi)\cdot\mathbf{t}\,ds'\\&=-2\Omega\int_0^s\mathbf{n}\cdot\nabla\phi\,ds',\end{aligned} \tag{15}$$

with s denoting arc-length and $\mathbf{t}$ the unit tangent. $B(0,t)$ can be absorbed in the usual way by defining a new potential:

$$\bar{\phi}\equiv\phi-\int_0^t B(0,t')\,dt'. \tag{16}$$

The overbar is suppressed hereafter. Note that $B(0,t)$ is *not* an arbitrary function of time. It is related to the mechanical energy of a reference point on the drop circumference. Nevertheless, $B(0,t)$ is a function of time only and can be absorbed into a velocity potential.

Equations (15)–(16), (13), and (6) combine into an integro-differential Bernoulli equation for the evolution of the free surface shape:

$$\begin{aligned}-2H\frac{\sigma}{\rho}+\frac{\partial\phi}{\partial t}+\frac{1}{2}(\nabla\phi)^2-\frac{1}{2}(\Omega f)^2+\Omega\frac{\partial\phi}{\partial\theta}\\=-2\Omega\int_0^s\mathbf{n}\cdot\nabla\phi\,ds' \qquad \text{on } S(t).\end{aligned} \tag{17}$$

Thus the finite amplitude oscillations of the inviscid two-dimensional drop rotating at fixed angular velocity are found by solving Laplace's equation (9) in the drop volume (10) that evolves according to the nonlinear, integro-differential Bernoulli equation (17) at the drop surface (11). The arc-length integral in Eq. (17) couples *all* parts of the drop surface and the solution method appropriate in this situation is quite different from those used when the drop does not rotate (e.g., [25 or 26]).

It is appropriate to measure length in units of the radius R of the unperturbed drop and time in units of a natural period $\sqrt{\rho R^3/\sigma}$. The corresponding dimensionless variables are

$$\tilde{\mathbf{x}} = \mathbf{x}/R, \qquad \tilde{t} = t(\sigma/\rho R^3)^{1/2}, \qquad \tilde{\Omega} = \Omega(\rho R^3/\sigma)^{1/2}, \qquad \tilde{\phi} = \phi(\rho/\sigma R)^{1/2}. \tag{18}$$

These are the variables used hereafter but the tildes are omitted.

In Appendix A, we prove that total energy and angular momentum are conserved by the two-dimensional rotating and oscillating drops. In Appendix B, we derive the weak or Galerkin form of the equations of drop motion.

3. TIME INTEGRATION

3.1. *Algorithm*

After substituting the finite element representations (57)–(59) (Appendix B) for the velocity potential, the free surface location and the global coordinates, as well as their partial derivatives with respect to ξ and η, the Galerkin/finite element residuals (67)–(68) become a set of nonlinear ordinary differential equations in time that can be expressed as

$$R_i(\boldsymbol{\alpha}, \boldsymbol{\beta}, \dot{\boldsymbol{\alpha}}) = 0, \quad i \in \{N\}, \qquad R_j^*(\boldsymbol{\alpha}, \boldsymbol{\beta}, \dot{\boldsymbol{\alpha}}, \dot{\boldsymbol{\beta}}) = 0, \quad j \in \{N_B\}, \tag{19}$$

where $\boldsymbol{\alpha} \equiv (\alpha_1, ..., \alpha_{N_B})$, etc. (Fig. 2). Time derivatives in Eq. (19) were discretized at the pth time step, $\Delta t_p = t_p - t_{p-1}$, by either first-order backward-differences (BD) or second-order trapezoid rule (TR),

$$\dot{\boldsymbol{\alpha}}(t_p) = c_1[\boldsymbol{\alpha}(t_p) - \boldsymbol{\alpha}(t_{p-1})]/\Delta t_p + c_2\dot{\boldsymbol{\alpha}}(t_{p-1}), \qquad \dot{\boldsymbol{\beta}}(t_p) = c_1[\boldsymbol{\beta}(t_p) - \boldsymbol{\beta}(t_{p-1})]/\Delta t_p + c_2\dot{\boldsymbol{\beta}}(t_{p-1}). \tag{20}$$

Here $c_1 = 1$, $c_2 = 0$ for backward-differences, $c_1 = 2$, $c_2 = -1$ for the trapezoid rule and $\boldsymbol{\alpha}(t_{p-1})$, $\dot{\boldsymbol{\alpha}}(t_{p-1})$, etc. are known from the previous time step.

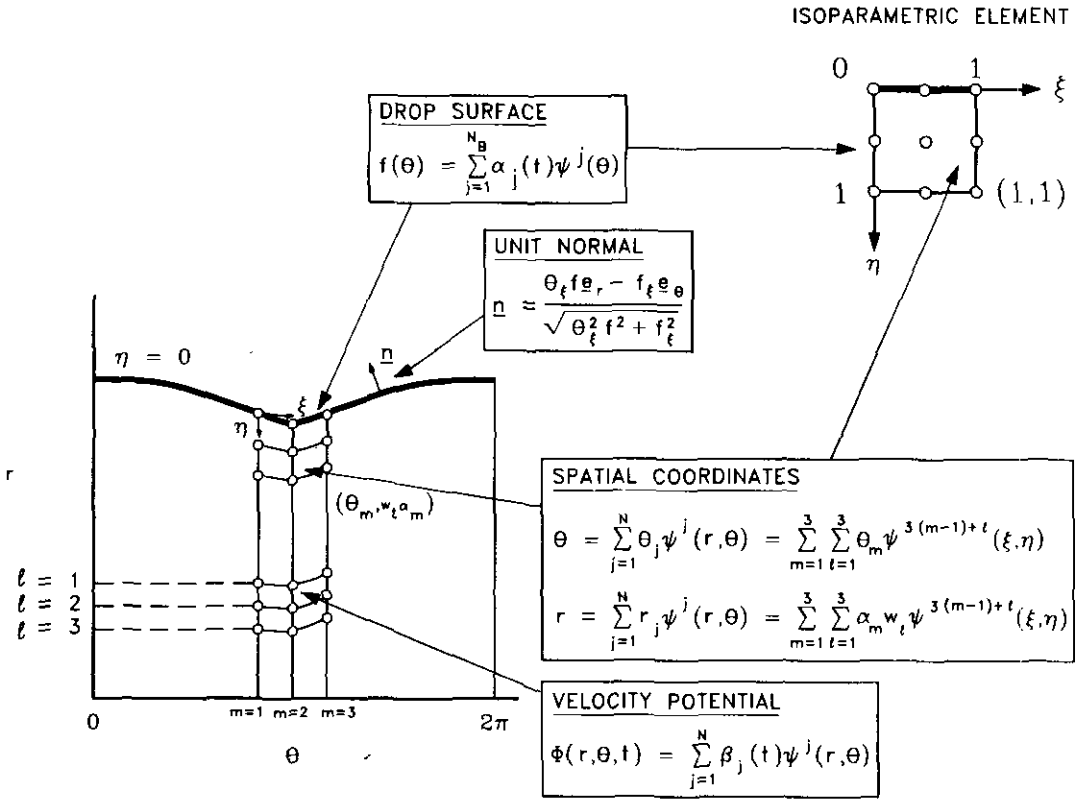

FIG. 2. Spatial and isoparametric finite elements.

Time discretization (20) reduces Eqs. (19) to a set of nonlinear algebraic equations. At every time step, these equations were solved by Newton iteration that updates the vectors of unknown coefficients $\boldsymbol{\alpha}(t)$ and $\boldsymbol{\beta}(t)$ by means of the Jacobian matrix of partial derivatives:

$$\begin{bmatrix} \frac{\partial R_i}{\partial \alpha_m} & \vdots & \frac{\partial R_i}{\partial \beta_k} \\ \cdots\cdots & \vdots & \cdots\cdots \\ \frac{\partial R_j^*}{\partial \alpha_m} & \vdots & \frac{\partial R_j^*}{\partial \beta_k} \end{bmatrix} \begin{bmatrix} \Delta\alpha_m \\ \cdots \\ \Delta\beta_k \end{bmatrix} = - \begin{bmatrix} R_i \\ \cdots \\ R_j^* \end{bmatrix}. \tag{21}$$

The derivation of the elements of the Jacobian or "stiffness" matrix from Eqs. (67)–(68) is tedious but straightforward.

The initial condition chosen was that of an undeformed drop suffering a disturbance in velocity potential proportional to the nth harmonic:

$$\begin{aligned} &f(\theta, 0) = 1 \\ &\phi(r, \theta, 0) = \phi_n r^n \cos n\theta, \qquad \phi_n \geqslant 0, \quad n = 2, 3, 4 \cdots . \end{aligned} \tag{22}$$

A first-order forward difference predictor,

$$\begin{aligned} \boldsymbol{\alpha}(t_{p+1}) &= \boldsymbol{\alpha}(t_p) + \mathring{\boldsymbol{\alpha}}(t_p)\, \Delta t_{p+1}, \\ \boldsymbol{\beta}(t_{p+1}) &= \boldsymbol{\beta}(t_p) + \mathring{\boldsymbol{\beta}}(t_p)\, \Delta t_{p+1}, \end{aligned} \tag{23}$$

was used with the backward-difference method. A second-order Adams–Bashforth predictor,

$$\begin{aligned} \boldsymbol{\alpha}(t_{p+1}) &= \boldsymbol{\alpha}(t_p) + \frac{\Delta t_{p+1}}{2} \\ &\quad \times \left[\left(2 + \frac{\Delta t_{p+1}}{\Delta t_p} \right) \mathring{\boldsymbol{\alpha}}(t_p) - \frac{\Delta t_{p+1}}{\Delta t_p} \mathring{\boldsymbol{\alpha}}(t_{p-1}) \right] \\ \boldsymbol{\beta}(t_{p+1}) &= \boldsymbol{\beta}(t_p) + \frac{\Delta t_{p+1}}{2} \\ &\quad \times \left[\left(2 + \frac{\Delta t_{p+1}}{\Delta t_p} \right) \mathring{\boldsymbol{\beta}}(t_p) - \frac{\Delta t_{p+1}}{\Delta t_p} \mathring{\boldsymbol{\beta}}(t_{p-1}) \right], \end{aligned} \tag{24}$$

was used with the trapezoid rule. The L_∞ norm of the correction provided by Newton iteration, $\|d_{p+1}\|_\infty$, was an estimate of the local time truncation error of the trapezoid rule [13]. Time steps were chosen adaptively by requiring the norm of the time truncation error at the next time step to be equal to a prescribed value, ε_t,

$$\Delta t_{p+1} = \Delta t_p (\varepsilon_t / \|d_{p+1}\|_\infty)^{1/3}. \tag{25}$$

Relative error of 0.1 % per time step ($\varepsilon_t = 10^{-3}$) was set, and at each time step usually two, but occasionally up to eleven, Newton iterations were necessary to keep the corrector error below 10^{-6}.

Equations (21) were solved in double precision on an IBM RS6000, Model 530, workstation with Hood's [16] frontal solver modified by Silliman [33], Walters [36] and Kheshgi and Scriven [17]. A typical run required 8192 time steps (cf. Appendix C), a mesh of $N_\theta \times N_r = 48 \times 8$ or 96×16 finite elements with biquadratic basis functions ($2N_\theta \times (2N_r + 2) = 1728$ or 6528 unknowns), and between 12 and 48 CPU hours.

3.2. *Solution Filtering*

By means of computational experiments, we established an approximate region of the phase space (Ω, ϕ_n) for each wave number n in which up to 24 backward-difference time steps with a fixed time increment $\Delta t_p = 0.0005$ were sufficient to smooth initial conditions (22) before the second-order trapezoid rule integration was used. The number of these fixed time steps increased with the rotation rate, disturbace amplitude and the initial wave number, and was significantly higher than that suggested in [23] and also that used in [25]. For example, for $n = 2$, this region is bounded from above by the following points (Ω, ϕ_2): $(0, \phi_2 < \infty)$, (1, 0.7), (2, 0.4), (2.449, 0.1). Outside of this region *no* degree of initial smoothing by backward-differencing was sufficient to prevent the solution from diverging at some later time t_{max}. For example, when $\Omega = 2$ and $\phi_2 = 0.5$, Figure 3 shows that this dimensionless time was $t_{\max} = 68.354$. As the last three shapes in Figure 3 were less than 2×10^{-6} time units apart, the loss of solution was catastrophic. When $\Omega = 2$ and $\phi_2 = 0.7$, the solution diverged at $t_{\max} = 4.335$. Thus, for $\Omega = 2$, the numerical

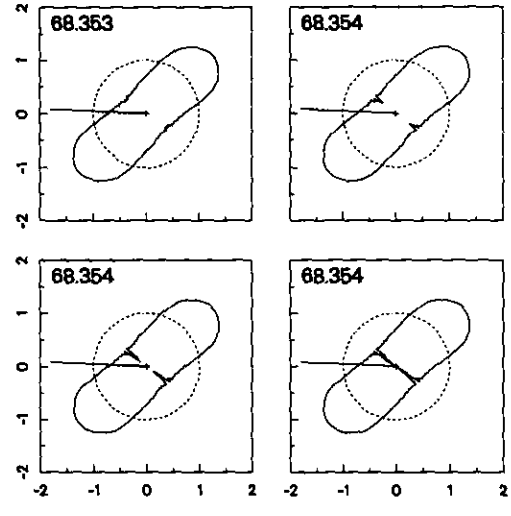

FIG. 3. Catastrophic growth of a random perturbation in the initial conditions of drop motion caused by roundoff error when $\Omega = 2$ and $\phi_2 = 0.5$; the last three shapes are less than 2×10^{-6} time units apart. The solid line rotates with the solid-body rotation.

algorithm was able to follow the motion of the rotating oscillating drop slightly longer than 21 full rotations when $\phi_2 = 0.5$, but barely longer than one rotation when $\phi_2 = 0.7$.

Insight into the cause of this behavior was gained by analyzing the coefficients of the Fourier expansion of drop shapes calculated on a mesh with $N_\theta \times N_r = 48 \times 8$ elements. The highest frequency ("zigzag" mode) resolved by such a mesh is $n = 24$, therefore the Fourier expansion of the drop shape with 24 terms is sufficient to fully represent the solution. In theory, since the initial disturbance in velocity potential has only one ($n = 2$) Fourier coefficient different from zero, the drop shape's Fourier coefficients at small times should decay at least exponentially with increasing wave number. In practice, the spectrum seen by the computer stops decaying because of roundoff error, turning the Fourier coefficients for $n > 4$ into random noise. This noise in the initial drop shape amounts to a spurious perturbation of the desired initial condition (22). The amplitudes of all wave number modes increase as time increases, but they generally decrease as n increases at a given time. As already noted by Krasny [19] and Lundgren and Mansour [22], increasing the number of elements in the mesh only worsens the problem for a fixed machine accuracy. This is because, with more elements, higher wave numbers are represented. Once spuriously perturbed by roundoff error, these amplify quicker, leading to a faster collapse of the solution.

Much like Krasny [19], we assert that a computational noise is introduced by the machine representation of the initial condition's spectrum and (1) expand the drop shape function $f(\theta, t)$, or velocity potential at the free surface into a truncated Fourier series

$$f_N(\theta, t_p) = 1 + a_0(t_p) + \sum_{n=1}^{N_\theta/2} a_n(t_p) \cos n\theta + b_n(t_p) \sin n\theta, \tag{26}$$

at the end of every time step t_p, (2) set to zero all Fourier coefficients $a_n(t_p)$ and $b_n(t_p)$ whose amplitude is less than this noise level ε_n,

$$f_N(\theta, t_p) \to f_{\varepsilon_n}(\theta, t_p), \tag{27}$$

and (3) replace the calculated drop shape by its *filtered* Fourier expansion,

$$f(\theta_i, t_p) = f_{\varepsilon_n}(\theta_i, t_p), \qquad i = 1, \cdots, 2N_\theta . \tag{28}$$

The coefficients of Fourier expansion are evaluated using the same interpolation and integration procedures as those used to integrate the finite element residuals and the Jacobian. In order for an oscillation mode to grow, its amplitude must exceed the noise level in a single time step and once this has happened for every mode, the filter *turns off* and the computation proceeds normally. This technique is well illustrated by the solution for $\Omega = 2$ and $\phi_2 = 0.5$. With the noise level set to $\varepsilon_n = 10^{-10}$, the filter turned off permanently at $t = 0.12361$. As time advances, the unfiltered and filtered solution *gradually* diverge from each other. For example, a plot of the "middle" ($n = 12$) cosine harmonic, Fig. 4, shows that over the first 10 time units the two solutions are almost identical. Yet between 58 and 68 time units, Fig. 5 shows that the filtered solution is different *and* markedly smoother than the unfiltered one, and, moreover, as shown in Fig. 6, the spurious high frequency waves are absent in the filtered drop shapes. The computational advantage of using the initial filter can be significant. After 6871 time steps, the elapsed time of the filtered solution is 30% longer than that of the failed unfiltered one. When the

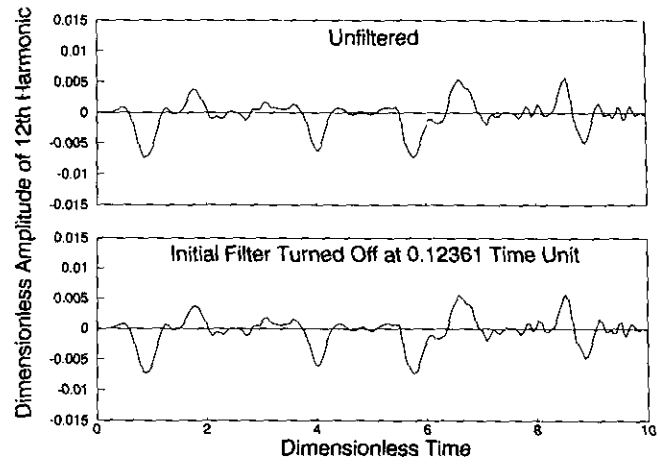

FIG. 4. When $\Omega = 2$ and $\phi_2 = 0.5$, the amplitudes of the "middle" (12th) cosine harmonic of the unfiltered (top) and initially filtered (bottom) drop shapes are almost identical for $t \leqslant 10$.

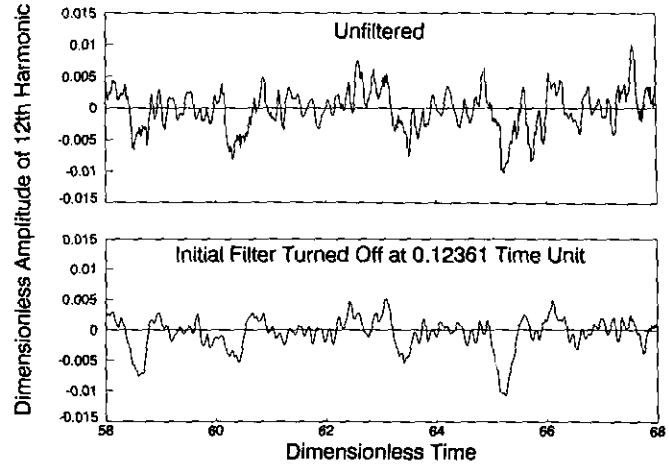

FIG. 5. When $\Omega = 2$ and $\phi_2 = 0.5$, the amplitudes of the "middle" (12th) cosine harmonic of the unfiltered (top) and initially filtered (bottom) drop shapes become very different as time progresses ($t > 58$). Note the high frequency noise present in the unfiltered shapes.

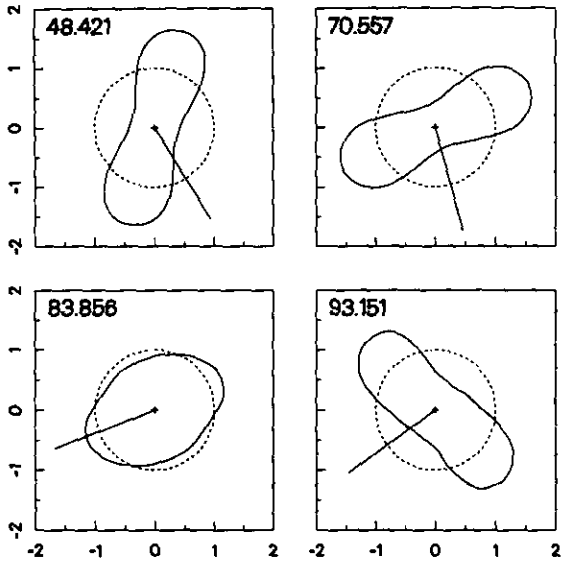

FIG. 6. The high frequency noise present in the unfiltered drop shapes when $\Omega = 2$ and $\phi_2 = 0.5$ (cf. Fig. 3) is effectively removed by the initial Fourier filter. The solid line rotates with the solid-body rotation.

filter was active, the approximation error measured at the end of every time step as

$$\sqrt{\sum_{i=1}^{2N_\theta} [f(\theta_i, t_p) - f_{\epsilon_n}(\theta_i, t_p)]^2}, \tag{29}$$

was less than 10^{-4}. The effects of initial filtering are gradual and subtle. In contrast, when the drop shape (or velocity potential) is filtered at every time step, the solution eventually becomes distorted; this is an important issue to which we return to in Section 4.5.

It is worthwhile to note that solution filtering was *unnecessary* in the absence of rotation, regardless of the initial disturbance amplitude. Indeed, as shown in Fig. 7, when $\Omega = 0$, filtering was unnecessary even for a solution that ultimately failed due to drop breakup. This observation is consistent with our previous results for axisymmetric free drops [25], where four backward-difference time steps sufficed to smooth the initial conditions. This work supersedes, however, our earlier results for the two-dimensional rotating drops [4–5]. There, the insufficient mesh resolution and the short elapsed times of calculations suppressed the high-frequency transients and thus did not allow us to realize that we had problems with convergence.

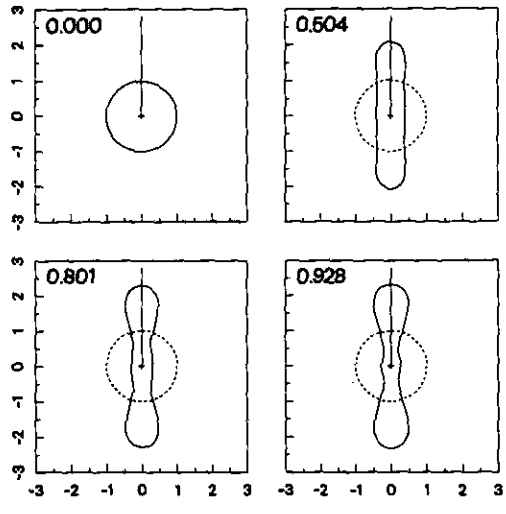

FIG. 7. Breakup of a cylindrical nonrotating drop ($\Omega = 0$) caused by an initial disturbance of amplitude $\phi_2 = 1.21$.

4. RESULTS

4.1. *Linear Theory*

The computed dynamic response of an inviscid cylindrical drop to an nth harmonic disturbance in velocity potential having small amplitude ϕ_n was compared with predictions of linear theory. The linear response to such a disturbance [14],

$$\begin{aligned} \phi(r, \theta, t) &= \phi_n r^n \cos[n\theta - (n-1)\,\Omega t] \cos(\alpha t), \\ &\quad \phi_n \ll 1, \\ f(\theta, t) &= 1 + \frac{n\phi_n}{\alpha^2 - \Omega^2} \{\alpha \cos[n\theta - (n-1)\,\Omega t] \\ &\quad \times \sin(\alpha t) - \Omega \sin[n\theta - (n-1)\,\Omega t] \cos(\alpha t)\}, \\ \alpha &\equiv \sqrt{(n-1)[n(n+1) - \Omega^2]}, \end{aligned} \tag{30}$$

is governed by a pair of angular velocities

$$\omega_{n\pm} = (n-1)\Omega \pm \alpha. \tag{31}$$

Note that the initial condition for the drop shape in this work, $f(\theta, 0) = 1$, differs from Eq. (30) evaluated at $t = 0$. Therefore, the numerical calculation goes through an initial transient during which the drop shape "catches up" with the disturbance in velocity potential. Indeed, the initial conditions (22) correspond to a pressure impulse that sets into oscillation a gyrostatically rotating drop.

The real parts of $\omega_\pm$ are the phase velocities of disturbances of wave number n and their imaginary parts determine whether the disturbances grow or decay. When $\omega_\pm$ is complex, the oscillation is unstable, because one mode grows in time while the other decays. The condition for stable oscillations is that $\omega_\pm$ be real, or that $\Omega \leqslant \sqrt{n(n+1)}$. Thus instability of the cylindrical rotating drop of inviscid liquid to the second cylindrical harmonic is predicted for $\Omega \geqslant \sqrt{6} = 2.4494897\ldots$. Figure 8 shows the variation of $\omega_\pm$ for $n = 2$ with the angular velocity of rotation $\Omega \leqslant \sqrt{6}$. Because the wave corresponding to ω_+ travels around the cylinder at a rate that exceeds the angular velocity of rota-

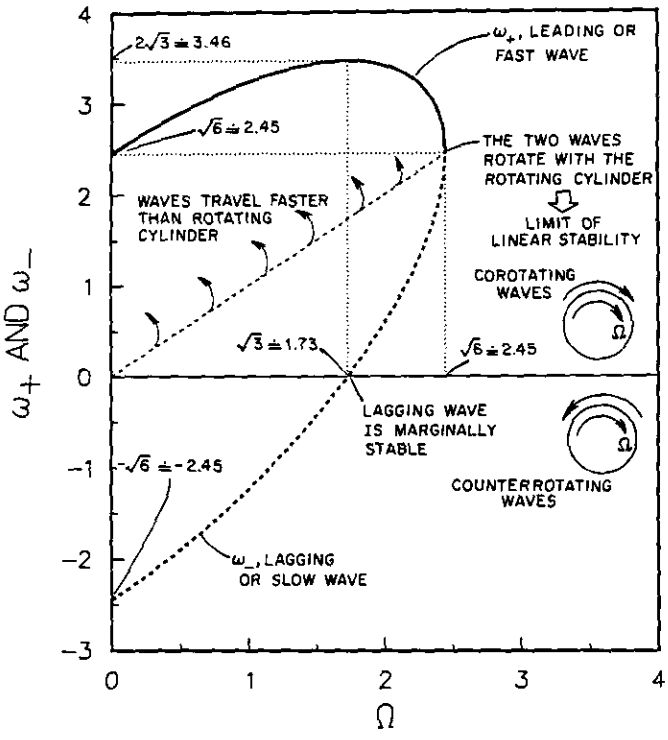

FIG. 8. The variation of the angular velocities of oscillations ω_+ and ω_- with the angular velocity of rotation Ω for $n = 2$.

tion Ω, it is called a leading or fast wave. Similarly, the wave corresponding to ω_- is called a lagging or slow wave. When the angular velocity of rotation exceeds $\sqrt{n+1}$, the lagging waves, too, travel in the direction of the rotation and approach the leading waves. When the rate of rotation attains $\sqrt{n(n+1)}$, the leading and lagging waves travel around the cylinder at equal angular velocities. At this point, as the linearized analysis of [14] first showed and the finite element results of this paper confirm, the cylinder becomes neutrally stable to an n-lobed ($n = 2, 3, \ldots$) perturbation. Thus, translationally symmetric, inviscid liquid drops rotating at angular velocities exceeding $\sqrt{n(n+1)}$ are unstable to infinitesimal-amplitude disturbances, though they succumb sooner to finite-amplitude disturbances. Interestingly, close to the linear stability limit, e.g., when $\Omega = 2.4490$, and with a small-amplitude initial disturbance, e.g., $\phi_2 = 0.1$, the drop oscillations were stable for 8192 timesteps ($t_{\max} = 349.031$), but the computed oscillation amplitude was as large as 0.4.

Just like electrical charge, rotation changes the dynamics of drop motion by allowing resonances between different normal modes. This occurs whenever

$$\omega_{m\pm} = k\omega_{n\pm}, \qquad k \geq 2, \quad m > n. \tag{32}$$

This is shown in Figure 9. For example, the slow wave $\omega_{5-} = 5$ resonates with two slow waves, ω_{10-} and ω_{15-}, at two different angular velocities Ω. Most of these resonances are weak ($k > 2$), and develop only gradually through nonlinear mode coupling when the drop oscillation is started by a single-mode impulse, as in Eq. (22). Therefore, the ability to follow the drop motion for *very* long times is essential.

4.2. *Nonlinear Oscillations*

In this paper, angular velocities $\omega_\pm$ of drop oscillations were found by Fourier spectral analysis of the free surface motion at fixed θ, e.g., $f(0, t)$ (see Appendix C). The Fourier

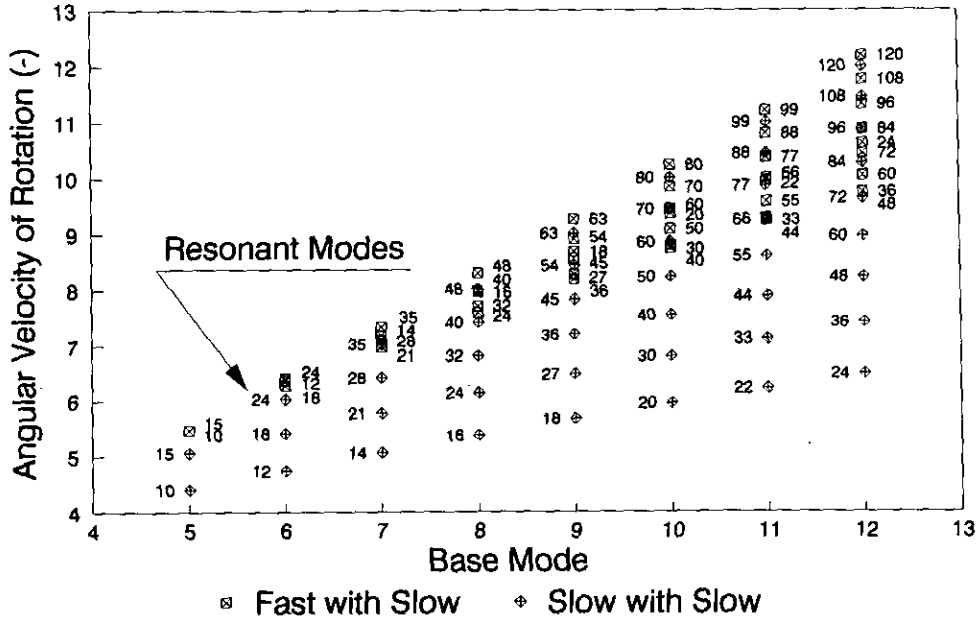

FIG. 9. Mode coupling for the translationally symmetric rotating drop; resonance of normal modes.

power spectra presented here were calculated with a modification of the standard routine **spectrm**( ) in [28].

Sample results for the drop response to $\phi_2 = 0.1$, 0.2, 0.4, and 0.5 are shown in Fig. 10 when $\Omega = 1$. Absolute values of dominant frequencies $|\omega_\pm|$, normalized to 1 for convenience, are those that correspond to maxima in the Fourier power spectra. The frequency resolution, equal to $\frac{1}{2}$ of the uniform spacing between sampled frequencies, is shown as error bars in Figs. 11 and 12. These error bars increase with the disturbance amplitude because the elapsed time of oscillation decreases when the total number of time steps is held fixed (8192). First, we note that the calculated response to small amplitude disturbances agrees well with the linear theory. Second, as with oscillating axisymmetric drops [35, 25], the absolute values of the angular velocities of both waves decrease as the disturbance amplitude increases. This decrease is approximately quadratic over the range of ϕ_2 values studied. It is noteworthy that the fast waves slow down at a higher rate than the slow ones: this suggests that at *any* rotation velocity below the linear stability limit ($\Omega < \sqrt{6}$), the drop will become unstable for an initial disturbance amplitude large enough to cause both waves to resonate.

4.3. *Conservation of Mass, Energy, and Angular Momentum*

As the disturbance amplitude increases, the dominant frequencies shift and the numerical results can no longer be compared with prediction of linear theory. Instead, we test how nearly constant is the drop volume V, and how nearly vanishing is mass flow $Q(t)$ across the drop surface in the plane of oscillation:

$$V(t) = \frac{1}{2}\int_0^{2\pi} f^2\, d\theta,$$
$$Q(t) = \int_0^{2\pi} \left(\phi_r - \frac{f_\theta}{f^2}\phi_\theta - \mathring{f} - \Omega f_\theta\right) f\, d\theta. \tag{33}$$

Here volume is measured in units of R^3 and mass flux in units of $\sqrt{\sigma\rho R^3}$. For moderate and large amplitude oscillations reported in this paper, the fluctuations in drop volume

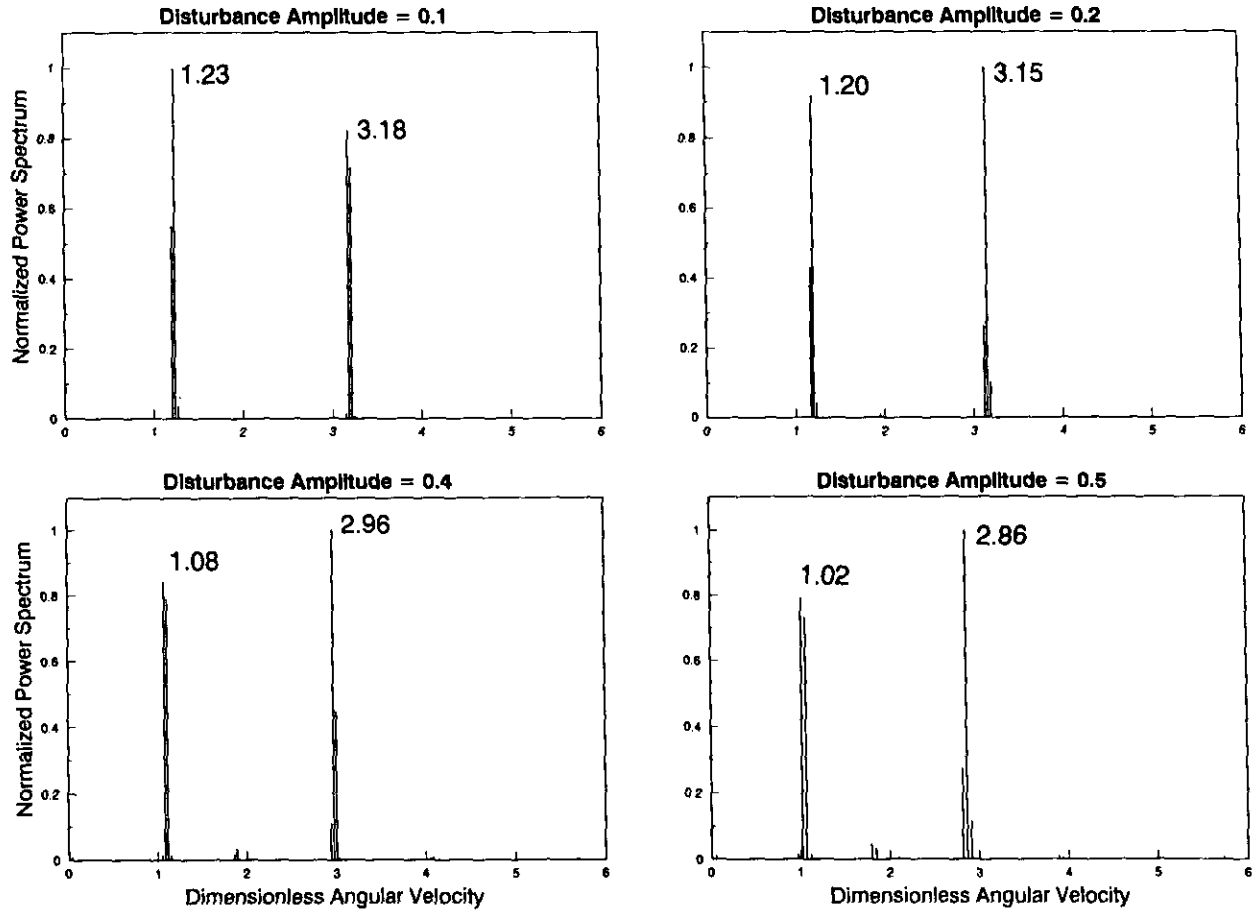

FIG. 10. The normalized Fourier power spectra when $\Omega = 1$ and for $\phi_2 = 0.1$, 0.2, 0.4, and 0.5. Note the tight frequency resolution afforded by the long elapsed oscillation times (see Appendix A).

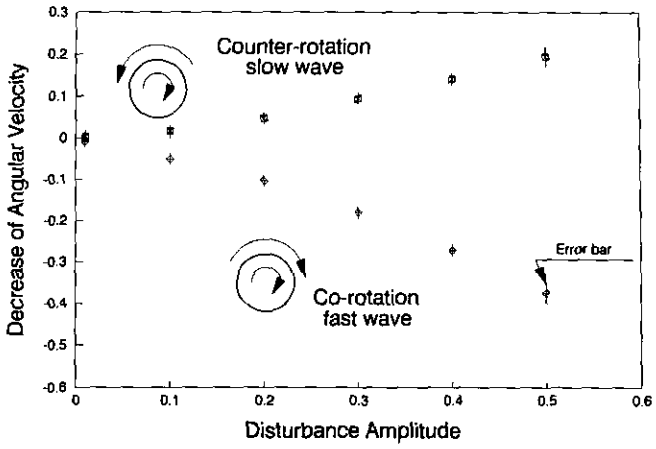

FIG. 11. The decrease of the angular velocity of oscillations with initial disturbance amplitude ϕ_2 when $\Omega = 1$; initial impulse, second cylindrical harmonic.

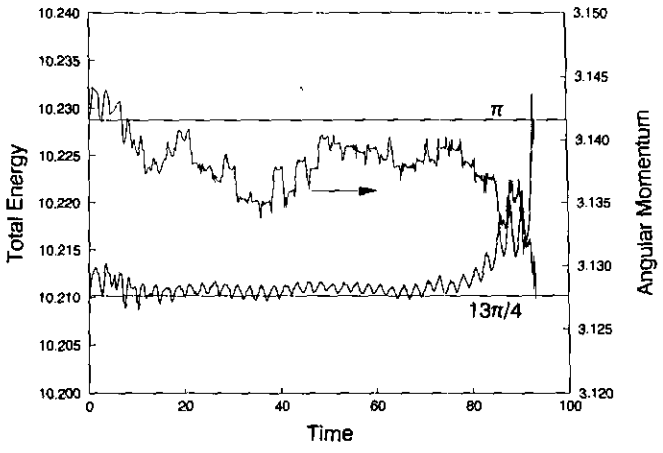

FIG. 13. Within the numerical accuracy, a translationally symmetric cylindrical drop, rotating at fixed angular velocity, conserves both energy and angular momentum!; $\Omega = 2$, $\phi_2 = 0.5$.

and mass flux across the interface were of the order of 4×10^{-4} and 10^{-10}, respectively, i.e., they were less than the time truncation error ε_t.

In an inertial frame of reference, the total energy of a rotating drop can be split into kinetic and surface energy contributions:

$$E_K(t) = \frac{1}{2}\int_0^{2\pi}\int_0^{f} (\Omega r \mathbf{e}_\theta + \nabla\phi)^2 \, r \, dr \, d\theta$$

$$= \frac{1}{2}\int_0^{2\pi}\int_0^{f}\left[\Omega^2 r^2 + \left(\phi_r^2 + \frac{\phi_\theta^2}{r^2}\right) + 2\Omega\phi_\theta\right] \times r \, dr \, d\theta, \tag{34}$$

$$E_S(t) = \int_0^{2\pi} \sqrt{f^2 + f_\theta^2}\, d\theta \tag{35}$$

(in units of σR^2). The drop's angular momentum is

$$L(t) = \int_0^{2\pi}\int_0^{f} (\Omega r^2 + \phi_\theta)\, r \, dr \, d\theta \tag{36}$$

(in units of $\sqrt{\sigma\rho R^7}$). Equation (34) has three terms. The first one is the kinetic energy of rotation, the second is the kinetic energy of the disturbance velocity, and the third one is the interaction between the rigid body rotation and the disturbance velocity in the θ-direction. The first two terms are positive-definite, whereas the third one *is* negative, as shown below. Depending on Ω, the components of kinetic energy are either in phase or out of phase.

As shown in Appendix A, total energy of the drop is always conserved, and so is its angular momentum. Figure 13 shows that for $\Omega = 2$ and $\phi_2 = 0.5$, the total drop energy and angular momentum are conserved to within 2×10^{-4}

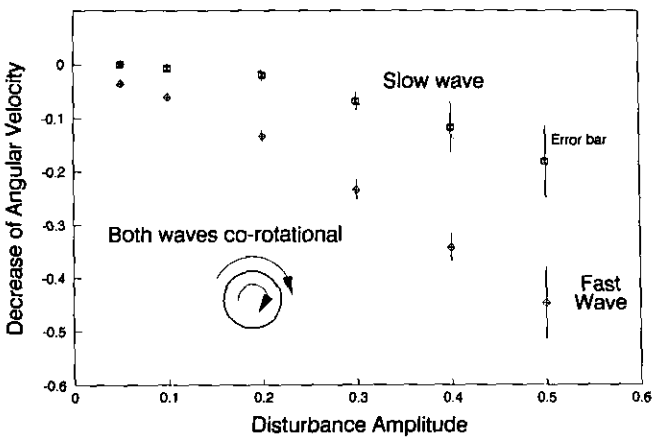

FIG. 12. The decrease of the angular velocity of oscillations with initial disturbance amplitude ϕ_2 when $\Omega = 2$; initial impulse, second cylindrical harmonic.

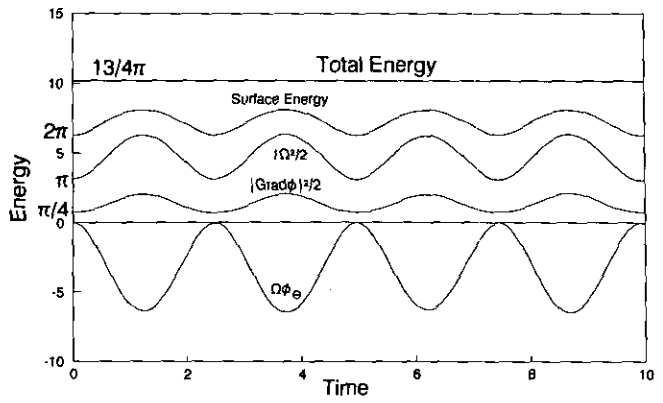

FIG. 14. The three components of the kinetic energy plus the surface energy add up to a constant total energy of $13\pi/4$ when $\Omega = 2$ and $\phi_2 = 0.5$, as predicted from linear theory, and remain so throughout the entire simulation *only* because energy is conserved. On the other hand, the oscillation frequency is markedly lower than that of linear oscillations.

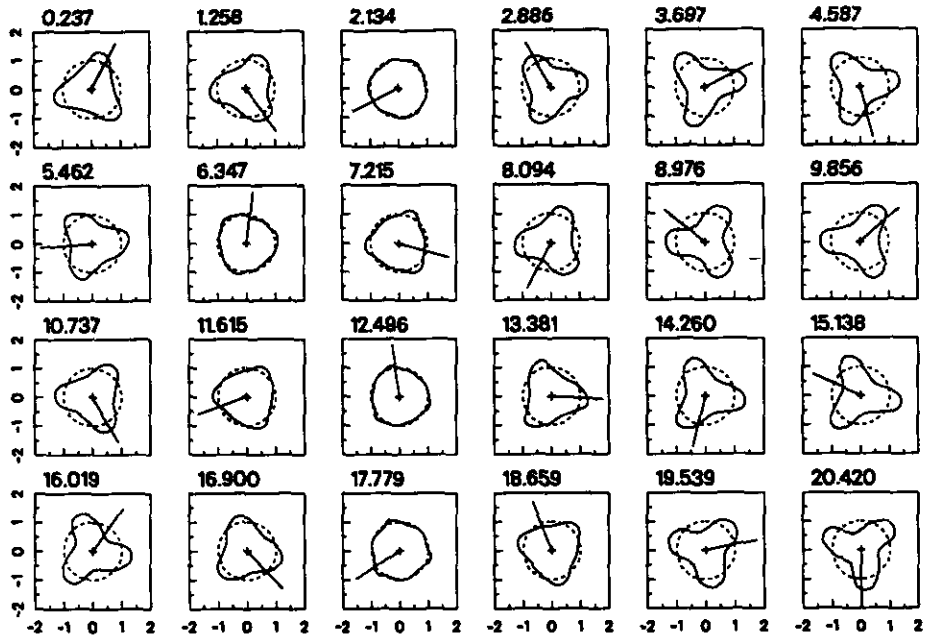

FIG. 15. A sequence of *unfiltered* drop shapes when $\Omega = 2$ and $\phi_3 = 0.5$. The elapsed time t is listed above each drop shape. The solid line rotates with the solid-body rotation and is *not* followed by the drop shapes because of the presence of running waves.

and 2×10^{-3}, respectively. The initially filtered solution begins to loose accuracy after 80 units of time.

It can be shown that with the initial conditions (22), the total energy and angular momentum of the drop are

$$E_t = \tfrac{1}{4}(2n\phi_n^2 + \Omega^2)\pi + 2\pi, \tag{37}$$

and

$$L_z = \tfrac{1}{2}\pi\Omega. \tag{38}$$

For $n = 2$, one can show that the three components of the kinetic energy are

$$E_K(t) \approx \tfrac{1}{4}\pi\Omega^2 + O(\phi_2^2) + \pi\phi_2^2 + O(\phi_2^4) - \frac{4\pi\Omega^2}{\alpha^2}\phi_2^2 \sin^2(\alpha t) - O(\phi_2^4). \tag{39}$$

Similarly, surface energy is

$$E_S(t) \approx 2\pi + O(\phi_2^2). \tag{40}$$

The components of the total drop energy are shown in Fig. 14 for $\Omega = 2$ and $\phi_2 = 0.5$.

4.4. *Drop Shapes and Pressures*

Two sequences of drop shapes for the following initial conditions: $\Omega = 2$ and $\phi_3 = 0.5$, and $\Omega = 1$ and $\phi_4 = 0.5$, are shown in Figs. 15–18. These solutions were *not* filtered and in both cases a high frequency noise lead to the eventual solution breakdown at $t > 20$ and 35, respectively.

The pressure field in the drop is obtained from Eqs. (11)–(12) as a by-product of the finite element calculations and lends further insight into the physics. All pressure fields in Fig. 19 were calculated when the oscillation had closely approached its full amplitude. Figure 19a shows that the pressure field inside a slightly perturbed drop, $\phi_2 = 0.1$, rotating at angular velocity $\Omega = 1$ at time $t = 0.643$, qualitatively follows that predicted by the linear theory:

$$p = \tfrac{1}{2}\Omega r^2 + \mathrm{Re}\{i\phi_n r^n e^{i(n\theta - \omega_\pm t)}[(n-2)\Omega - \omega_\pm]\}. \tag{41}$$

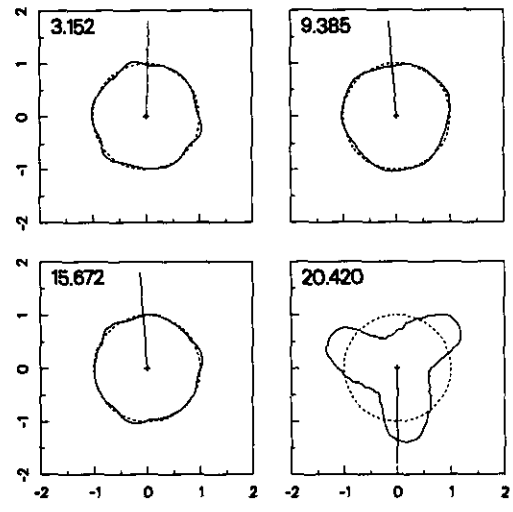

FIG. 16. An enlargement of selected drop shapes in Fig. 15 reveals a high frequency noise leading to solution breakdown at $t = 20.420$. The solid line rotates with the solid-body rotation; $\Omega = 2$; $\phi_3 = 0.5$.

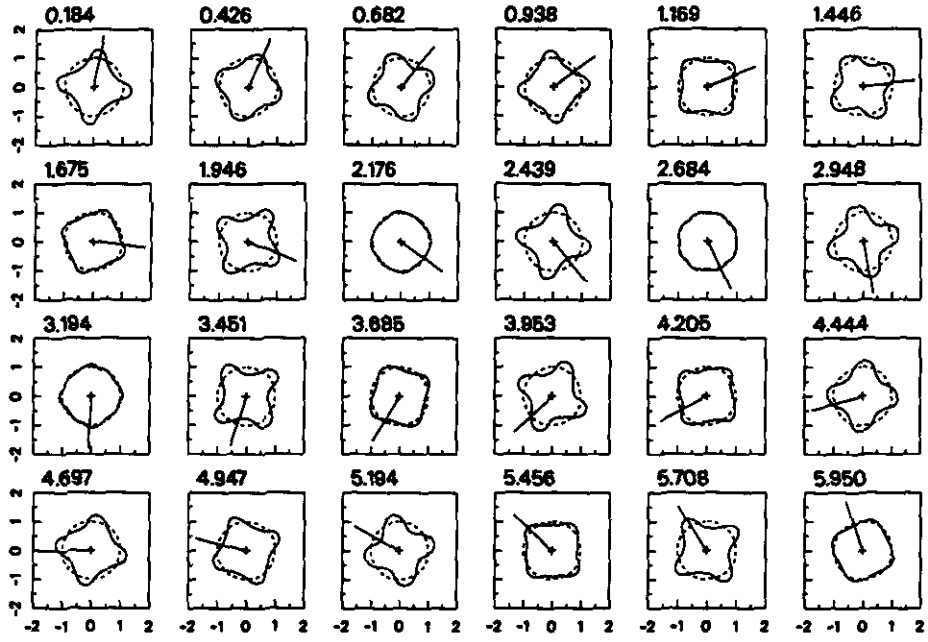

FIG. 17. A sequence of *unfiltered* drop shapes when $\Omega = 1$ and $\phi_4 = 0.5$. The elapsed time t is listed above each drop shape. The rotating line rotates with the solid-body rotation and is *not* followed by the drop shapes because of the presence of running waves.

In such a drop, the isobars can be plotted as the concentric circles generated by the gyrostatic pressure, $\frac{1}{2}\Omega r^2$, and deformed by the oscillatory pressure, $\mathrm{Re}\{i\phi_n r^n\, e^{i(n\theta-\omega_\pm t)}[(n-2)\Omega-\omega_\pm]\}$, the latter being proportional to the disturbance amplitude, ϕ_n, and rising as r^n until the free surface is reached, i.e., as $r \to f$. As a result, the isobars not only get denser, but they also deviate from their gyrostatic shape as the drop surface is approached. Nonlinearity of the large amplitude oscillations (Figs. 19b–c) is now apparent; the isobars in highly deformed drops, $\phi_2 \geq 0.5$, are concentrated near the crests of the waves and become distorted by mode coupling.

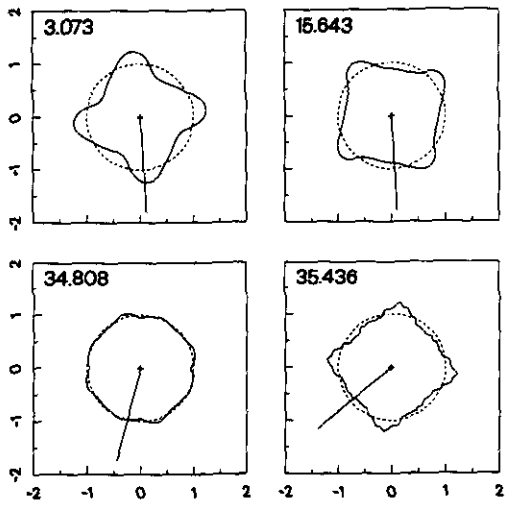

FIG. 18. An enlargement of selected drop shapes in Fig. 17 reveals a high frequency noise leading to the solution breakdown at $t = 35.436$. The solid line rotates with the solid-body rotation; $\Omega = 1$, $\phi_4 = 0.5$.

4.5. *Comparison with Boundary Element Methods*

In free surface flow problems, numerous other smoothing techniques have been employed over the years, such as the five- and seven-point smoothing techniques [21], regridding [10], and curvature damping [24]. In a more recent paper, Pelekasis *et al.* [26] used a boundary element (BE) method to solve Laplace's equation inside a nonrotating axisymmetrical drop and a finite element (FE) method to solve the equations describing the evolution of the drop surface. In that work, both artificial viscosity and a fourth-order surface diffusion technique (following [22]) were used to dampen high frequency noise. It is significant that none of the boundary element algorithms above employed the initial Fourier filtering [19], a technique also used in this work. We suspect that this is caused by inherent instabilities in these algorithms which are due to the BE technique being used in conjunction with explicit methods of time integration; evidently, these algorithms require smoothing at every time step to avoid failure. Pelekasis *et al.* [26] give the most thorough comparison of various BE techniques to date. In the BE part of their algorithm, Pelekasis *at al.* use the direct application of Green's theorem to obtain a Fredholm integral equation of the first kind and

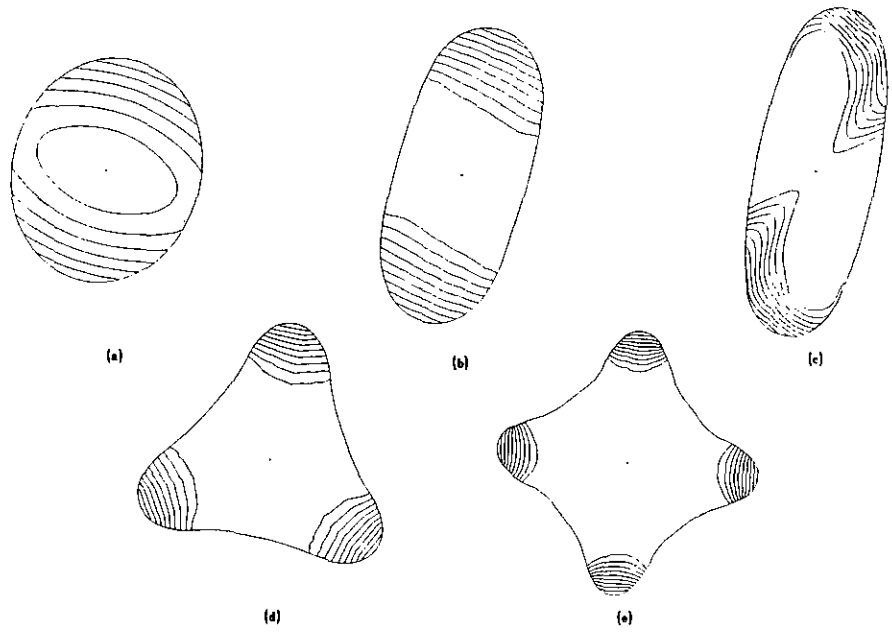

FIG. 19. Pressure fields inside drops rotating at angular velocity $\Omega = 1$. Isobars taken at equal intervals in pressure for: (a) $\phi_2 = 0.1$, $t = 0.643$; (b) $\phi_2 = 0.5$, $t = 0.560$; (c) $\phi_2 = 0.9$, $t = 0.335$; (d) $\phi_3 = 0.5$, $t = 0.268$; (e) $\phi_4 = 0.5$, $t = 0.162$.

an indirect formulation, using a distribution of dipoles, that leads to a Fredholm integral equation of the second kind. They use both quadratic and B-spline basis functions and carry integration in time with explicit schemes with constant time steps. Although these authors mention an implicit scheme, they do not discuss predictions based on it. Pelekasis *et al.* then compare the direct and indirect methods, each with quadratic or B-spline basis functions, and with and without continuous numerical filtering. The authors carry their calculations with 21, 26, 41, 51, 81, and 101 nodes to $t \approx 2$, and sometimes $t \approx 8$, claiming that these are very long integration times necessary to capture the nonlinear effects as accurately as possible. By way of contrast, our simulations are carried out to $t = 100$ or even $t = 350$ to achieve the desired level of accuracy in the Fourier spectrum (Appendix C) and to test the stability of our algorithm.

To compare our FE method with the hybrid BE/FE methods described by Pelekasis *et al.*, we calculated the drop motion resulting from an initial disturbance in velocity potential proportional to the fourth cylindrical harmonic with amplitude $\phi_4 = 0.3$. Two general cases were considered: (1) a drop rotating at $\Omega = 2$ and (2) a nonrotating drop $\Omega = 0$. For the case of the rotating drop, case (1), the filtering was applied to the initial drop shape and the filter turned itself off when the amplitude of every mode exceeded the noise level, as described in Section 3.2. For the case of the nonrotating drop, case (2), three subcases were considered: (2a) calculations were carried out without the filter; (2b) the filter was forced to be on for the first 50 time steps; and (2c) the filter was forced to be on at every time step. Moreover, all of the previous cases were forced to run for 8192 time steps. For the rotating drop, the simulation reached a time of $t = 140$ after 8192 time steps. This took 32 h of CPU time to complete or, equivalently, 822 CPU seconds per time unit. The initial filter turned itself off after six time steps at $t = 0.020207$. The energy was conserved within 0.09% and the angular momentum within 0.15% (Fig. 20). In the case of the nonrotating oscillating drop (2a), Fig. 21, the total elapsed time of the simulation was $t = 208$, which took 32 h of CPU time, or 554 CPU seconds per time unit. The total energy was conserved to within

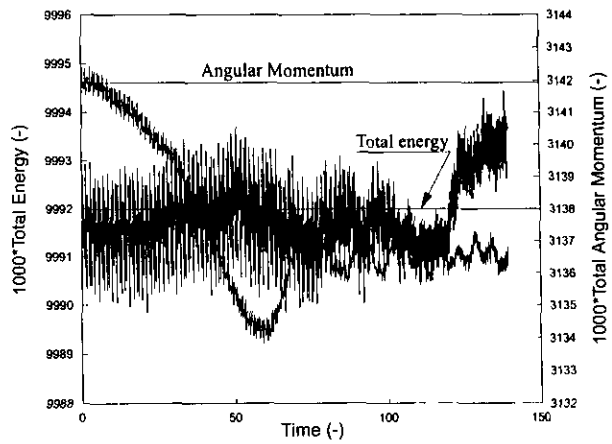

FIG. 20. Conservation of total mechanical energy and angular momentum when $\Omega = 2$ and $\phi_4 = 0.3$. Here the initial filter turns itself off after the sixth time step.

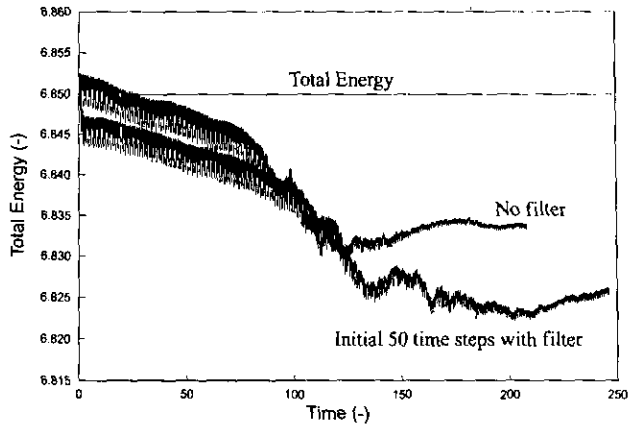

FIG. 21. Conservation of total mechanical energy when $\Omega = 0$ and $\phi_4 = 0.3$. Here there is either no fitering or the initial filter is forced on for the first 50 time steps (8192 time steps total).

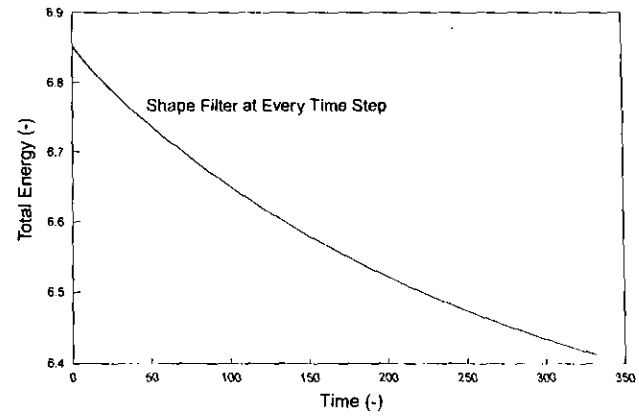

FIG. 22. Conservation of total mechanical energy when $\Omega = 0$ and $\phi_4 = 0.3$. Here the shape filter is forced on at every time step. Note the 6.7% loss in energy, and the smoothness of the solution (8192 time steps).

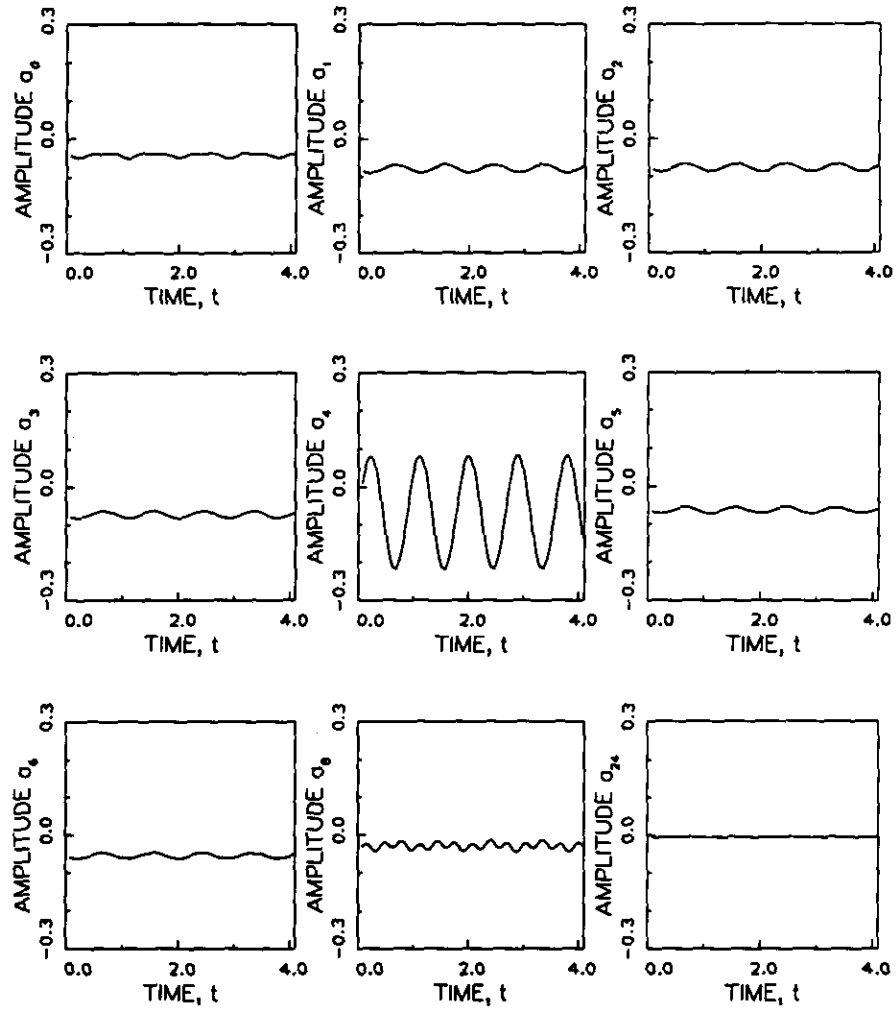

FIG. 23. Decomposition of drop shapes into linear modes when $\Omega = 0$, $\phi_4 = 0.3$, $t \leqslant 4$, and no filter is used.

0.20%. In Case 2b, Fig. 21, the total simulation time was $t = 246$, which took 32 CPU hours, or 468 CPU seconds per time unit. The total energy was conserved to within 2%. In contrast, in Case 2c, the total simulation time was $t = 332$, which took 24 h of CPU time or 260 CPU seconds per time unit. In this case, the time step was artificially limited (to be consistent with the other runs) from increasing even further. However, 6.5% of the total energy was lost during this simulation, as shown in Fig. 22. Figures 23 and 24 show that numerical solutions in Cases 2b and 2c are virtually identical within the first four time units, but they evolve in dramatically different ways as time progresses, as shown in Figs. 25 and 26. We therefore caution that accuracy and stability comparisons of the short-time solutions obtained with different numerical methods will often be invalid for the long-time solutions. We propose that such comparisons should be made for a *fixed* dimensionless time of oscillation or for a fixed number of oscillation periods. We also caution that extensive solution filtering that must be employed by various algorithms that have appeared in the literature is bound to cause the long-time response of the simulated system to differ from that of the actual physical system, a serious problem.

Although direct comparison of our algorithm with those of others is often unfair to our algorithm because we use larger oscillation amplitudes, and rotation introduces additional severe numerical difficulties, this is what we find:

- Our *implicit* algorithm uses an adaptive time step whose length depends on the severity of the problem and varies between 0.0005 (lower limit) to 0.5% of the minimum period of oscillations given by linear theory (upper limit for improved accuracy of Fourier spectra). On average, our time step is 0.01–0.08 of a time unit. This is several orders of magnitude larger than the constant time steps of 0.00025–0.008 used by Pelekasis *et al.* Evidently, this fact

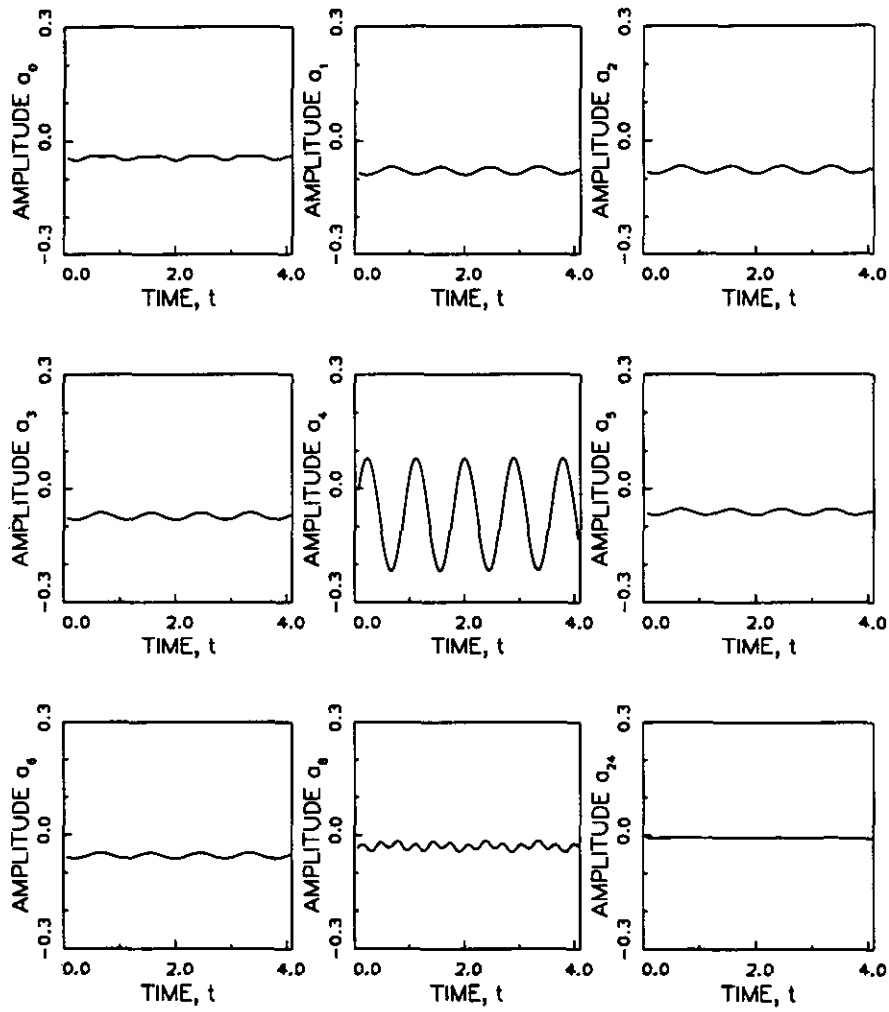

FIG. 24. Decomposition of drop shapes into linear modes when $\Omega = 0$, $\phi_4 = 0.3$, $t \leqslant 4$, and with the shape filter forced on at every time step. Note that the drop respose here seems to be identical to that shown in Fig. 23.

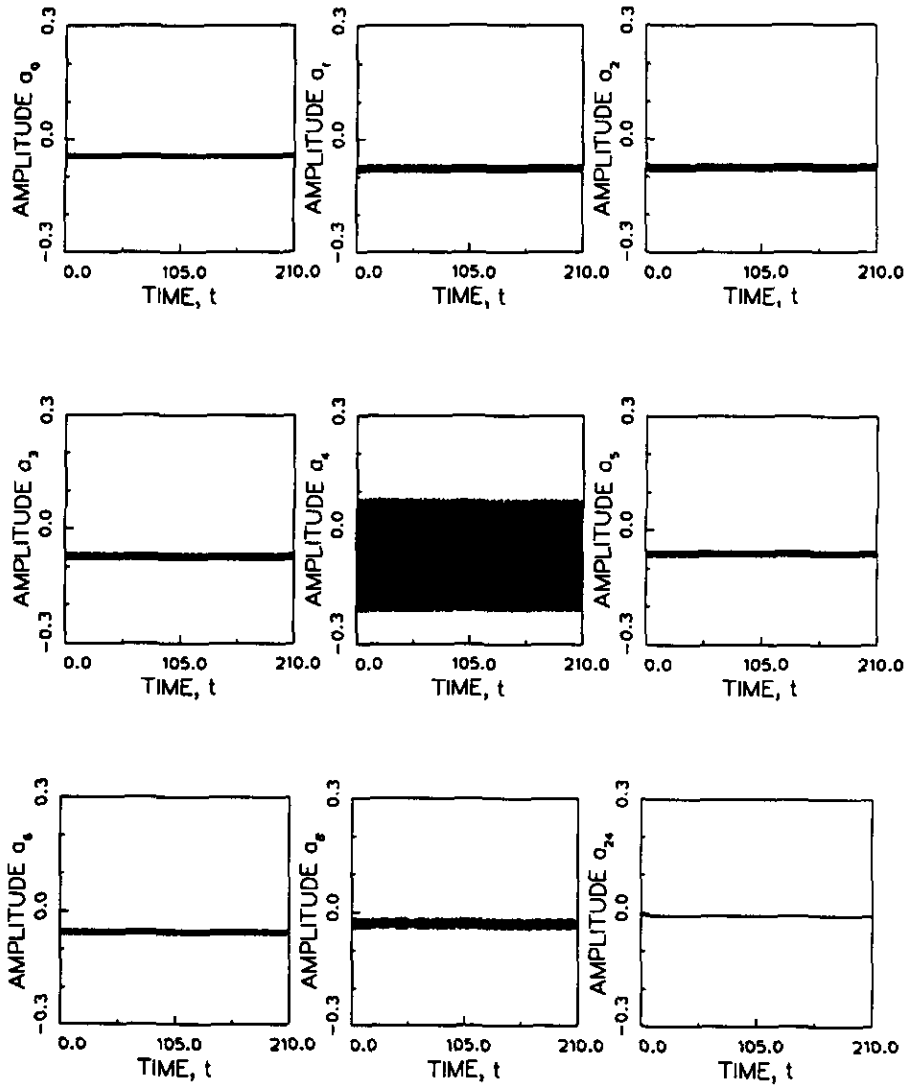

FIG. 25. Decomposition of drop shapes into linear modes when $\Omega = 0$, $\phi_4 = 0.3$, $t \leq 210$, and no filter is used. Note that energy is conserved and mode coupling develops.

plays a big role in offsetting the cost of inverting a matrix at each time step during our calculations over algorithms based on explicit methods which do not require solution of a system of algebraic equations, as shown below.

- With 96 surface nodes, our FE algorithm requires on average 2–5 s of CPU time per time step on the IBM RS6000, Model 530, versus 15-22 sec of CPU time on the IBM 3090 reported by Pelekasis *et al.* for 101 nodes. With fixed time steps $\Delta t = 0.001$, this translates into 14,500–21,750 CPU seconds *per time unit* on the IBM 3090 for the BE methods, as opposed to 200-900 CPU seconds per time unit on the IBM RS6000, Model 530 for our FE method. In other words, our method may be a factor of 100 more efficient than the BE methods discussed by Pelekasis *et al.* This comparison neglects the fact that the IBM 3090 is a supercomputer class machine that is faster than the IBM RS6000, Model 530.

- We use only the *initial* Fourier filter to cope with finite machine accuracy. The use of this filter is *unnecessary* within the first 10 time units of calculations, even for computing the strongly nonlinear oscillations of rotating drops. Moreover, the use of a filter is *never* necessary when the velocity of rotation is set to 0, a situation which more closely approximates the axisymmetric free drops considered by Pelekasis *et al.* In

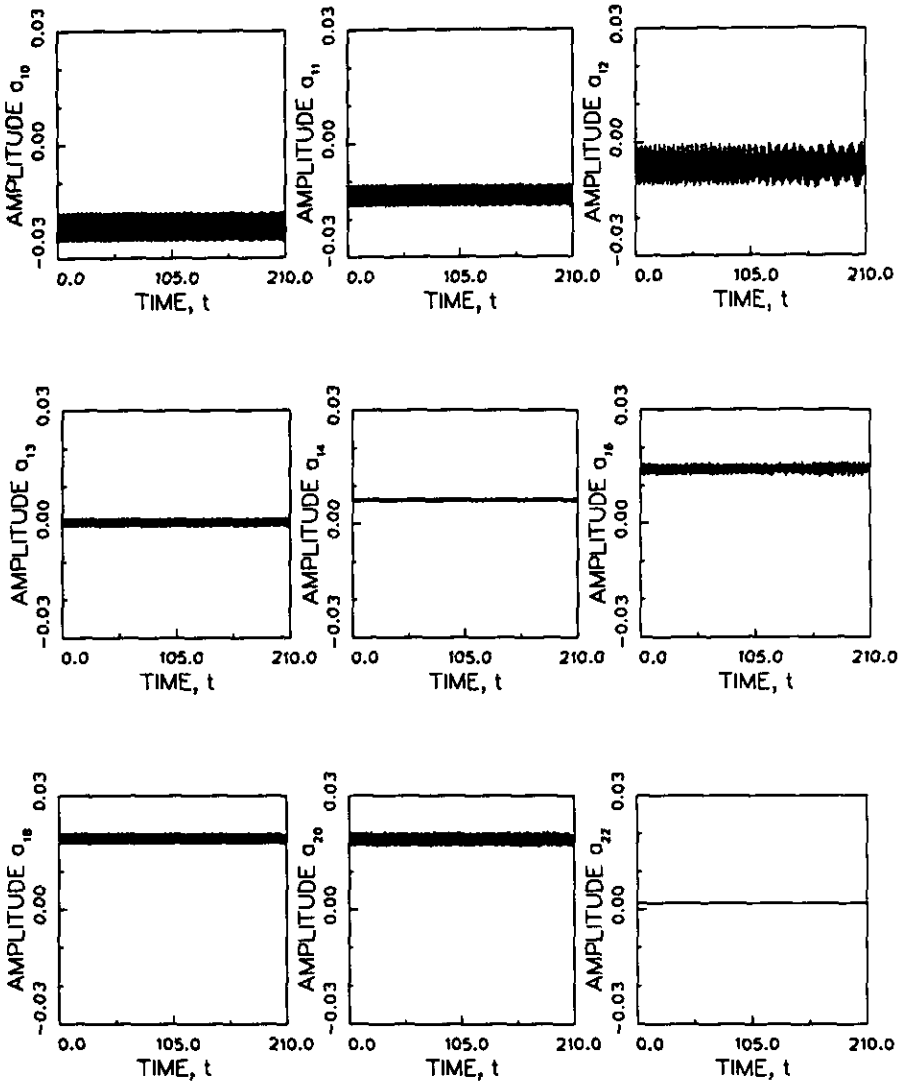

FIG. 25—*Continued*

contrast, the BE algorithms either fail catastrophically after two periods of oscillation (cf. Fig. 3 in [26]) or have to be smoothed after *every* time step. We assert that this repeated smoothing skews or even destroys the subtler features of the nonlinear dynamics, such as coupling between modes and weak resonances (see Figs. 25 and 26 and Section 4.1).

• Our criterion of solution failure which, for example, amounts to an increase of the total energy by 20 parts in 10,000, after as many as 80 time units (Fig. 13), is usually much more stringent than that listed in Table III of [26] after only 2 or 10 time units. It seems that the BE algorithms used by Pelekasis *et al.* are able to conserve total energy for a few periods of oscillation and rapidly deteriorate thereafter. Lundgren and Mansour's [22] method seems to be more robust, allowing in some cases time integration for up to 80 time units.

5. DISCUSSION

According to the foregoing results, the dynamics of a two-dimensional rotating drop is different from that of axisymmetric but nonrotating globular drops (cf. [22, 25, 26]). Particularly striking is the difference between the types of surface waves that can be seen along the interface separating the nonrotating and rotating drops from the surrounding

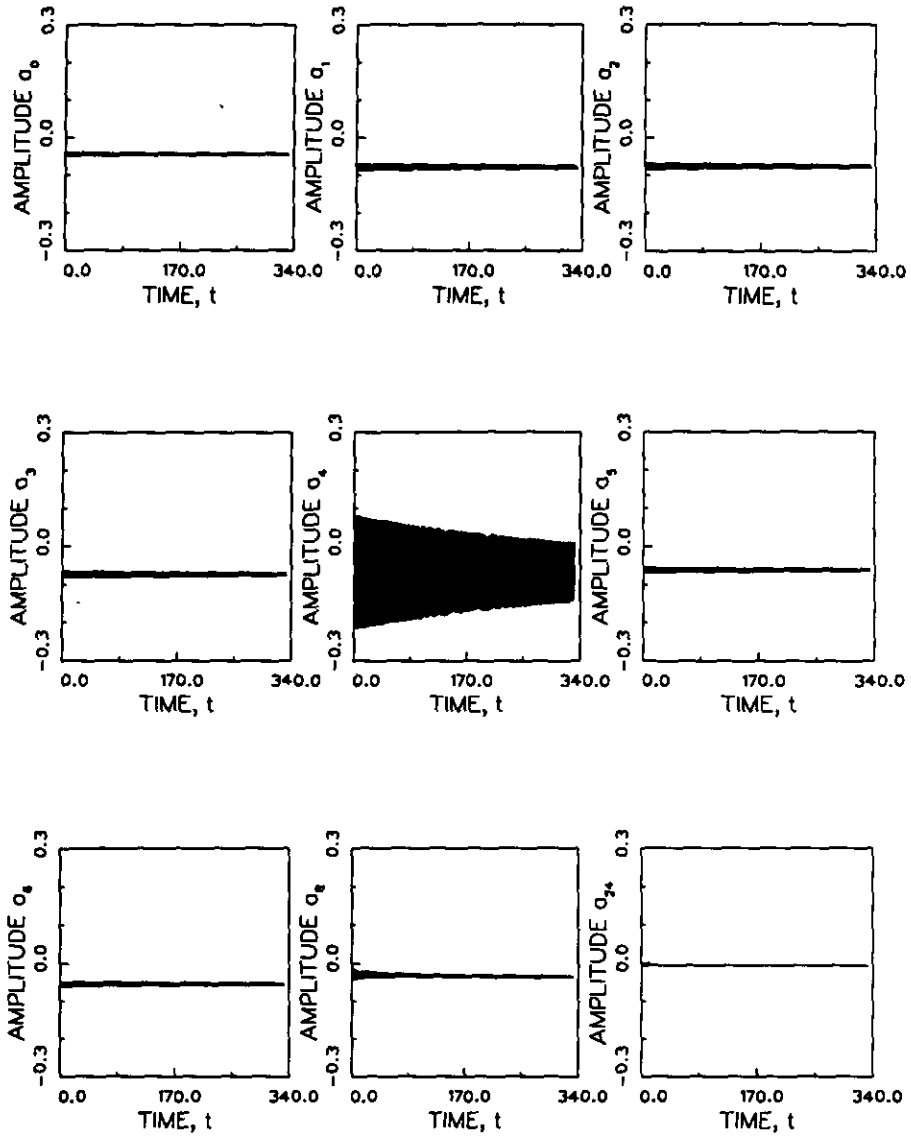

FIG. 26. Decomposition of drop shapes into linear modes when $\Omega = 0$, $\phi_s = 0.3$, $t \leqslant 332$, and the shape filter is forced on for 8192 time steps. Note that energy is *not* conserved and mode coupling is much weaker.

gas. The former drops display a much simpler pattern of standing waves, whereas the latter ones display an intricate pattern of traveling or running capillary waves. As the rotation rate increases, the amplitudes of these capillary waves grow.

The Galerkin/finite element method used here to determine the oscillations of rotating cylindrical drops is an extension to integro-differential equations of the "method of lines" successfully used in simulations of steady [18] and unsteady [17] viscous film flows, and large-amplitude oscillations of inviscid [25] and viscous [2] free drops. Modeling the breakup of cylindrical drops rotating at angular velocities *either* faster than $\sqrt{n(n+1)}$ while subjected to infinitesimal-amplitude disturbances *or* slower than $\sqrt{n(n+1)}$ while subjected to finite-amplitude disturbances should now be possible by merging the method presented in this paper with either of the two following techniques: (1) a composite coordinate system, which has already been used in [6] to follow gyrostatically rotating cylindrical drops all the way to breakup or (2) elliptic mesh generation, which allows easy discretization of domains of arbitrary shape [9].

The Fourier filtering of drop shapes at very early times is invaluable in removing noise from the initial conditions of

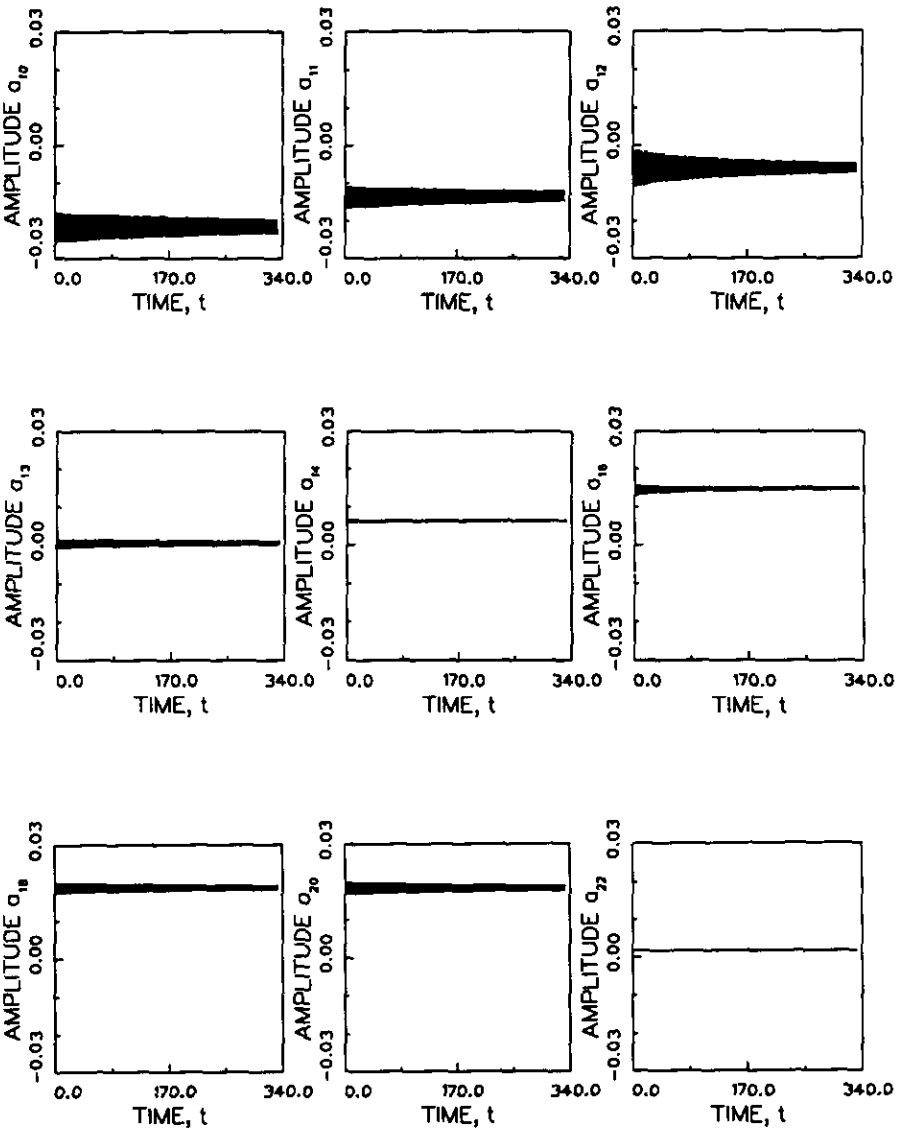

FIG. 26—*Continued*

drop motion caused by finite machine accuracy. Turning on the filter initially permits computation of the drop motion for tens or even hundreds of periods of oscillation, while at the same time drastically reducing computation time. Without the filter, the computations would ultimately break down for a variety of initial conditions.

In summary, our FE method is very competetive. In its present, constant spine, implementation, this method fails when the drop becomes too distorted. On the other hand, our method has superior stability, accuracy, and computational efficiency over several BE methods discussed in the literature.

APPENDIX A: CONSERVATION OF ENERGY AND ANGULAR MOMENTUM

The motion of a two-dimensional rotating drop conserves total mechanical energy, that is the sum of kinetic energy E_K and surface energy E_S. This result is counter-intuitive because the angular velocity of rotation also remains constant as the drop deforms. The mechanical energy balance is obtained by taking the scalar product of Eq. (3) with $\mathbf{v}$. After making use of translational symmetry of the drop motion, fluid incompressibility, and some rearrangement, one obtains

$$\frac{D}{Dt}\left(\frac{1}{2}\rho v^2\right) = -\mathbf{v}\cdot\nabla p. \tag{42}$$

To obtain total energy, we first integrate Eq. (42) over the volume of a unit length slice of the drop and use the Gauss theorem to transform the right-hand side into a surface integral over the entire *closed* surface of the slice $S_{tot} = S(t) + S_1 + S_2$, shown in Fig. 1. Then we use Eq. (6) to eliminate pressure along the drop surface $S(t)$, and note that translational symmetry requires $\mathbf{v}\cdot\mathbf{n}$ to vanish on both cylinder cross sections S_1 and S_2:

$$\frac{d}{dt}\int_V \frac{1}{2}\rho v^2\, dV = -\int_{S_{tot}} \mathbf{n}\cdot\mathbf{v}\, p\, dS$$

$$= \sigma\int_{S(t)} 2H\mathbf{v}\cdot\mathbf{n}\, dS. \tag{43}$$

The left side of Eq. (43) is the rate of change of kinetic energy dE_K/dt. Hence we need to show that the right side of (43) is the negative of the rate of change of surface energy. If the surface of the unit length slice of the drop is denoted by the vector $\mathbf{r}$ at time t, and the vector $\mathbf{r}' = \mathbf{r} + \delta\mathbf{r}$ at time $t + \delta t$, then the displacement of an element of surface area is [38]

$$\delta(dS) \equiv dS(t+\delta t) - dS(t) = \nabla_S\cdot\delta\mathbf{r}\, dS, \tag{44}$$

where the surface divergence ∇_S and the surface area element dS are evaluated on the undisplaced surface $S(t)$. Integration over the drop surface (per unit length) at time t and application of the surface divergence theorem (SDT) give

$$\delta S = \int_{S(t)} \delta(dS) = \int_{S(t)} \nabla_S\cdot\delta\mathbf{r}\, dS$$

$$= -\int_{S(t)} 2H\,\delta\mathbf{r}\cdot\mathbf{n}\, dS. \tag{45}$$

Line integrals that do arise from use of the SDT do not appear in Eq. (45) because translational symmetry requires that $\delta\mathbf{r}\cdot\mathbf{m} = 0$, $\mathbf{m}$ being the outward binormal unit vector along both edges of $S(t)$. Therefore, the total time derivative of the surface energy is

$$\frac{dE_S}{dt} = \sigma\frac{dS}{dt} = \sigma\frac{\delta S}{\delta t} = -\sigma\int_{S(t)} 2H\frac{\delta\mathbf{r}}{\delta t}\cdot\mathbf{n}\, dS$$

$$= -\sigma\int_{S(t)} 2H\mathbf{v}\cdot\mathbf{n}\, dS. \tag{46}$$

From Eqs. (46) and (43) it immediately follows that

$$\frac{d}{dt}(E_K + E_S) = 0. \tag{47}$$

Hence total energy is conserved during the translationally symmetric oscillations of incompressible, inviscid liquid drops.

Similarly, we can prove that total angular momentum $\mathbf{L}$ is conserved during the drop oscillations. The angular momentum balance is obtained by taking the vector product of Eq. (3) with $\mathbf{r}$. After some rearrangement:

$$\frac{D}{Dt}(\rho\mathbf{r}\times\mathbf{v}) = \nabla\times(p\mathbf{r}). \tag{48}$$

To obtain total angular momentum, we integrate Eq. (48) over the drop volume (per unit length) and use the Gauss theorem to transform the right-hand side into a surface integral. Then we use Eq. (6) to eliminate pressure along the drop surface and translational symmetry to eliminate contributions from both cross sections:

$$\frac{d\mathbf{L}}{dt} = \frac{d}{dt}\int_V \rho(\mathbf{r}\times\mathbf{v})\, dV = \int_{S_{tot}} \mathbf{n}\times\mathbf{r}p\, dS$$

$$= -\sigma\int_{S(t)} 2H\mathbf{n}\times\mathbf{r}\, dS. \tag{49}$$

The surface divergence theorem, together with translational symmetry, yields

$$-\int_{S(t)} 2H\mathbf{n}\times\mathbf{r}\, dS = \int_{S(t)} \nabla\times\mathbf{r}\, dS = \mathbf{0}. \tag{50}$$

Equations (50) and (49) prove that total angular momentum is conserved during the translationally symmetric oscillations of an inviscid, incompressible rotating drop:

$$\frac{d\mathbf{L}}{dt} = \mathbf{0}. \tag{51}$$

Without the requirement of translational symmetry, neither the total energy nor angular momentum of an oscillating drop rotating at constant angular velocity is conserved. This makes two-dimensional rotating liquid drops especially useful in testing the accuracy and long-time stability of numerical algorithms when oscillation amplitude is large and comparison with linear theory no longer holds.

APPENDIX B: REDUCTION TO GALERKIN FORM

The equations of drop motion in weak form are:

$$\int_V (\nabla^2\phi)\,\psi^i\,dV = 0, \qquad \psi^i(r,\theta)\in\{N\}, \tag{52}$$

$$\int_{S(t)}\left[\phi_t + \frac{1}{2}(\nabla\phi)^2 - \frac{1}{2}(\Omega f)^2 + \Omega\phi_\theta + 2\Omega\int_0^s \mathbf{n}\cdot\nabla\phi\,ds' - 2H\right] \times \mathbf{e}_r\cdot\mathbf{n}\,\psi^j\,dS = 0, \qquad \psi^j(\theta)\in\{N_B\}. \tag{53}$$

These can be reduced to first order with the use of Green's theorem,

$$\int_V \nabla\phi\cdot\nabla\psi^i\,dV - \int_{S(t)}\psi^i\mathbf{n}\cdot\nabla\phi\,dS = 0, \qquad \psi^i\in\{N\}, \tag{54}$$

and the surface divergence theorem [38],

$$\int_{S(t)}\left\{\left[\phi_t + \frac{1}{2}(\nabla\phi)^2 - \frac{1}{2}(\Omega f)^2 + \Omega\phi_\theta + 2\Omega\int_0^s \mathbf{n}\cdot\nabla\phi\,ds'\right] \times \mathbf{e}_r\cdot\mathbf{n}\,\psi^j + \nabla_S\cdot(\psi^j\mathbf{e}_r)\right\}dS = 0, \qquad \psi^j(\theta)\in\{N_B\}, \tag{55}$$

where

$$\nabla_S\cdot(\psi^j\mathbf{e}_r) = \frac{f_\theta\psi^j_\theta + f\psi^j}{f^2+f_\theta^2}, \qquad (\,)_v \equiv \frac{\partial(\,)}{\partial v}, \quad v = t,\theta,r. \tag{56}$$

$\{N\}$ is the set of N finite element basis functions ψ^i chosen to approximate velocity potential

$$\phi(r,\theta,t) = \sum_{i\in\{N\}}\beta_i(t)\,\psi^i(r,\theta), \tag{57}$$

and $\{N_B\}$ is a subset of $\{N\}$ that enumerates the free surface location

$$f(\theta,t) = \sum_{j\in\{N_B\}}\alpha_j(t)\,\psi^j(\theta). \tag{58}$$

Here β_i and α_j are the unknown and time-dependent coefficients of the approximation.

The weighting factor $\mathbf{e}_r\cdot\mathbf{n}$ in Eq. (53) helps to reduce twice the local mean curvature of the free surface, $2H$, to first order (cf. Eq. (7)). Equations (57)–(58), in turn, define partitions of the drop cross section in the (r,θ) plane into quadrilateral elements, each bordered by a pair of fixed spines, $\theta = \text{const}$, and a pair of curved sides that move in proportion to the free surface position,

$$r = \sum_{\substack{i\in\{N\}\\ j\in\{N_B\}}} r_i[\alpha_j(t)]\,\psi^i(r,\theta), \qquad \theta = \sum_{i\in\{N\}}\theta_i\psi^i(r,\theta), \tag{59}$$

where r_i and θ_i are the nodal values of r and θ; see Fig. 2. In this representation, values of r_i depend on the free surface shape, whereas those of θ_i do not. If N_r denotes the number of elements in the r-direction and N_θ is the number of elements in the θ-direction, then $N_B = 2N_\theta + 1$ and $N = (2N_r+1)(2N_\theta+1)$.

Because the integration is ultimately performed numerically in a fixed Cartesian coordinate system, the finite element approximations (57)–(58) are further mapped onto the unit square with coordinates $(\xi,\eta)\in[0,1]\times[0,1]$. The mapping is done by isoparametric transformation [34] of $r = r(\xi,\eta)$ and $\theta = \theta(\xi)$, and the Jacobian of this transformation

$$J \equiv \frac{\partial(r,\theta)}{\partial(\xi,\eta)} = \left(\frac{\partial\theta}{\partial\xi}\right)\left(\frac{\partial r}{\partial\eta}\right) \equiv \theta_\xi r_\eta \tag{60}$$

absorbs the evolution of the drop shape. θ does not depend on η because the spines are lines of constant θ:

$$\frac{\partial}{\partial\theta}(\,) = \frac{1}{\theta_\xi}\left[\frac{\partial}{\partial\xi}(\,) - \frac{r_\xi}{r_\eta}\frac{\partial}{\partial\eta}(\,)\right], \qquad \frac{\partial}{\partial r}(\,) = \frac{1}{r_\eta}\frac{\partial}{\partial\eta}(\,). \tag{61}$$

The corollary equations for free surface derivatives are even simpler, e.g.,

$$\frac{\partial f}{\partial\theta} = \frac{f_\xi}{\theta_\xi}. \tag{62}$$

In what follows, the subscripts ξ and η indicate differentiation with respect to these variables.

Finite element basis functions $\psi^i[r(\xi,\eta),\theta(\xi)]\in\{N\}$ and $\psi^j[\theta(\xi)]\in\{N_B\}$ are *locally* defined on the unit square and are also used to approximate the *global* coordinates r and θ:

$$r = \sum_{\substack{i\in\{N\}\\ j\in\{N_B\}}} r_i[\alpha_j(t)]\,\psi^i(\xi,\eta), \qquad \theta = \sum_{i\in\{N\}}\theta_i\psi^i(\xi,\eta), \tag{63}$$

Equations (55)–(56) require that the basis functions be at least continuous; therefore, the C^0 biquadratic basis functions $\psi^i(\xi, \eta)$, $i = 1, ..., 9$, and quadratic basis functions $\psi^j(\xi)$, $j = 1, 2, 3$, were used to approximate the velocity potential ϕ, the free surface location f, and the spatial coordinates r and θ (Fig. 2). Kinematic condition (5) is used to evaluate the surface integral in Eq. (55) and the line integral in Eq. (56),

$$\mathbf{n} \cdot \nabla\phi = \frac{f(\mathring{f} + \Omega f_\theta)}{\sqrt{f^2 + f_\theta^2}}. \tag{64}$$

Here $\mathring{f}$ is the time derivative of f, taken at fixed isoparametric coordinates. The surface $F \equiv r - f(\theta, t) = 0$ is material, hence its time derivative $dF/dt \equiv \partial F/\partial t + \mathbf{v}_s \cdot \nabla F = 0$. Inasmuch as $(\partial F/\partial t)_{r,\theta} = -(\partial f/\partial t)_{\xi,\eta} \equiv -\mathring{f}$ and $\nabla F = \mathbf{n}\sqrt{f^2 + f_\theta^2}/f$, Eq. (64) follows (cf. [17, 25]).

With Eqs. (56) and (64) substituted for $\nabla_S \cdot (\psi^j \mathbf{e}_r)$ and $\mathbf{n} \cdot \nabla\phi$, $dV = r\, dr\, d\theta\, dz$, $dS = \sqrt{f^2 + f_\theta^2}\, d\theta\, dz$, $ds' = \sqrt{f^2 + f_{\theta'}^2}\, d\theta'$, integration over $z \in [0, 1]$, and $\phi_t = \mathring{\phi} - \mathring{f}\phi_r$, Eqs. (54)–(55) become

$$\int_0^{2\pi} \int_0^f \nabla\phi \cdot \nabla\psi^i\, r\, dr\, d\theta - \int_0^{2\pi} f(\mathring{f} + \Omega f_\theta)\, \psi^i\, d\theta = 0, \qquad \psi^i \in \{N\}, \tag{65}$$

$$\int_0^{2\pi} \left\{ \left[\mathring{\phi} - \mathring{f}\phi_r + \frac{1}{2}(\nabla\phi)^2 - \frac{1}{2}(\Omega f)^2 + \Omega\phi_\theta + 2\Omega \int_0^\theta f(\mathring{f} + \Omega f_{\theta'})\, d\theta' \right] f\psi^j + \frac{f_\theta \psi^j_\theta + f\psi^j}{\sqrt{f^2 + f_\theta^2}} \right\} d\theta = 0, \qquad \psi^j \in \{N_B\}. \tag{66}$$

Finally, isoparametric transformation of Eqs. (65)–(66) yields the Galerkin/finite element residuals on a fixed, cartesian domain $(\xi, \eta) \in [0, 1] \times [0, 1]$:

$$R_i \equiv \theta_\xi \int_0^1 \int_0^1 \frac{\phi_\eta}{r_\eta} \psi^i_\eta\, r\, d\xi\, d\eta + \frac{1}{\theta_\xi} \int_0^1 \int_0^1 \left(\phi_\xi - \frac{r_\xi}{r_\eta}\phi_\eta \right) \left(\psi^i_\xi - \frac{r_\xi}{r_\eta}\psi^i_\eta \right) \frac{r_\eta}{r}\, d\xi\, d\eta + \int_0^1 (\theta_\xi \mathring{f} + \Omega f_\xi) f\psi^i\, d\xi, \qquad i \in \{N\}, \tag{67}$$

$$R_j^* \equiv \theta_\xi \int_0^1 \left[\mathring{\phi} - \mathring{f}\frac{\phi_\eta}{r_\eta} + \frac{1}{2}\left(\frac{\phi_\eta}{r_\eta}\right)^2 + \frac{1}{2\theta_\xi^2 f^2}\left(\phi_\xi - \frac{r_\xi}{r_\eta}\phi_\eta \right)^2 \right] f\psi^j\, d\xi + \int_0^1 \frac{f_\xi \psi^j_\xi + \theta_\xi^2 f\psi^j}{\sqrt{\theta_\xi^2 f^2 + f_\xi^2}}\, d\xi + \Omega \int_0^1 \left[\phi_\xi - \frac{r_\xi}{r_\eta}\phi_\eta - \frac{\Omega\theta}{2} f^2 \right] f\psi^j\, d\xi + 2\theta_\xi \Omega \int_0^1 \left[\int_0^\xi (\theta_\xi \mathring{f} + \Omega f_{\xi'}) f\, d\xi' + \sum_{\{N_f^*\}} \int_0^1 (\theta_\xi \mathring{f} + \Omega f_{\xi'}) f\, d\xi' \right] \times f\psi^j\, d\xi, \qquad j \in \{N_B\}. \tag{68}$$

It is noteworthy that the inner line integral in Eq. (68) has contributions from all free surface elements $\{N_f^*\}$ between $\theta = 0$ and the current θ, i.e., every free surface residual is coupled to all preceeding ones. To solve this problem, we have introduced a fictitious element that includes all free surface nodes. Every node in this additional element accumulates an appropriate portion of the line integral, which in turn is assembled simultaneously with the first two terms in Eq. (68). This approach has proven to be computationally efficient and relatively easy to program.

Specification of the initial shape of the free surface and the initial value of the velocity potential field

$$f(\theta, t = 0) = f_0(\theta), \qquad \phi(r, \theta, t = 0) = \phi_0(r, \theta), \tag{69}$$

and the periodicity of both the free surface shape and velocity potential field,

$$f(\theta = 0, t) = f(\theta = 2\pi, t), \qquad \phi(r, \theta = 0, t) = \phi(r, \theta = 2\pi, t), \tag{70}$$

complete the mathematical statement of the problem.

APPENDIX C: POWER SPECTRUM OF DROP OSCILLATIONS

Let T be the total time of drop oscillations, N the number of data sampling points (a power of 2), f_c the Nyquist frequency, Δf a sampling interval in frequency, Δ a constant sampling time interval, and $M = \frac{1}{4}N$ the size of data segments overlapping by one half of their length (to reduce the variance of the power spectrum estimate, [28]). Then

$$\Delta = \frac{T}{N - 1}, \tag{71}$$

$$f_c = \frac{1}{2\Delta}, \tag{72}$$

$$\Delta f = \frac{1}{Mf_c} = \frac{4}{N}\frac{N-1}{2T} \approx \frac{2}{T}. \tag{73}$$

The sampling interval for the angular frequency ω is

$$\Delta\omega = 2\pi\,\Delta f \approx \frac{4\pi}{T}. \tag{74}$$

To compare the results of numerical analysis to the linear theory, one should make the relative error

$$\varepsilon_T = \frac{\Delta\omega}{|(n-1)\Omega - \sqrt{(n-1)[n(n+1)-\Omega^2]}|}, \tag{75}$$

as small as possible. Combining Eqs. (74) and (75) then yields the elapsed time of drop oscillations required to achieve accuracy ε_T,

$$T \geqslant \frac{4\pi}{\varepsilon_T\,|(n-1)\Omega - \sqrt{(n-1)[n(n+1)-\Omega^2]}|}. \tag{76}$$

For example, if $\varepsilon_T = 0.01$ and $\Omega = 1$, then $T \geqslant 1016$.

REFERENCES

1. P. Annamalai, E. Trinh, and T. G. Wang, *J. Fluid Mech.* **158**, 317 (1985).
2. O. A. Basaran, *J. Fluid Mech.* **241**, 169 (1992).
3. G. K. Batchelor, *An Introduction to Fluid Dynamics* (Cambridge Univ. Press, Cambridge, UK, 1967).
4. R.E. Benner, T. W. Patzek, and L. E. Scriven, *Bull. Am. Phys. Soc.* **27** (9), 1168 (1982).
5. R. E. Benner, Ph.D. thesis, University of Minnesota, 1983 (unpublished).
6. R. E. Benner, O. A. Basaran, and L. E. Scriven, *Proc. R. Soc. London A* **433**, 81 (1991).
7. F. H. Busse, *J. Fluid Mech.* **142**, 1 (1984).
8. J. R. Carruthers and L. R. Testardi, *Annu. Rev. Mater. Sci.* **13**, 247 (1983).
9. K. N. Christodoulou and L. E. Scriven, *J. Comput. Phys.* **99**, 39 (1992).
10. D. G. Dommermuth and D. K. P. Yue, *J. Fluid Mech.* **178**, 195 (1987).
11. A. M. Gañán-Calvo, *J. Fluid Mech.* **226**, 63 (1991).
12. H. González, F. M. J. McCluskey, and A. Barrero, *J. Fluid Mech.* **206**, 545 (1989).
13. P. M. Gresho, R. L. Lee, and R. C. Sani, "On the Time-Dependent Solution of the Incompressible Navier–Stokes Equations in Two and Tree Dimensions," in *Recent Advances in Numerical Methods in Fluids*, edited by C. Taylor and K. Morgan, Vol. 1 (Pineridge Press, Swansea, UK, 1979), p. 27.
14. L. M. Hocking and D. H. Michael, *Mathematika* **6**, 25 (1959).
15. L. M. Hocking, The Stability of a Rigidly Rotating Column of Liquid, Mathematika **6**, 1–9 (1960).
16. P. Hood, *Int. J. Numer. Methods Eng.* **10**, 379 (1976); correction, *Int. J. Numer. Methods Eng.* **11**, 1055 (1977).
17. H. S. Kheshgi and L. E. Scriven, "Penalty Finite Element Analysis of Unsteady Free Surface Flows," in *Finite Elements in Fluids*, edited by J. T. Oden *et al.*, Vol. 5, (Wiley, New York, 1983), p. 393.
18. S. F. Kistler and L. E. Scriven, "Coating Flows," in *Computational Analysis of Polymer Processing*, edited by J. R. A. Pearson and S. M. Richardson, (Appl. Sci., London, 1983), p. 243.
19. R. Krasny, *J. Fluid Mech.* **167**, 65 (1986).
20. L. D. Landau and E. M. Lifshitz, "*Fluid Mechanics*," *Course of Theoretical Physics*, Vol. 6 (Pergamon Press, New York, 1960).
21. M. S. Longuet-Higgins and E. D. Cokelet, *Proc. R. Soc. London A* **350**, 1 (1976).
22. T. S. Lundgren and N. N. Mansour, *J. Fluid Mech.* **194**, 479 (1988).
23. M. Luskin and R. Rannacher, *Appl. Anal.* **14**, 117 (1982).
24. H. N. Oğuz and A. Prosperetti, *J. Fluid Mech.* **219**, 143 (1990).
25. T. W. Patzek, R. E. Benner, O. A. Basaran, and L. E. Scriven, *J. Comput. Phys.* **97**, 489 (1991).
26. N. A. Pelekasis, J. A. Tsamopoulos, and G. D. Manolis, *J. Comput. Phys.* **101**, 231 (1992).
27. J. A. F. Plateau, *Statique Experimentale et Theorique de Liquides Soumis aux Seules Forces Moleculaires* (Gauthier–Villars, Paris, 1873).
28. W. H. Press, B. P. Flannery, S. A. Teukolsky, and W. T. Vetterling, *Numerical Recipes in C, The Art of Scientific Computing* (Cambridge Univ. Press, Cambridge, UK, 1988).
29. Lord Rayleigh, *Proc. London Math. Soc.* **10**, 4 (1879).
30. Lord Rayleigh, *Philos. Mag.* **34**, 145 (1892).
31. W. K. Rhim, S. K. Chung, and D. D. Elleman, in *Proceedings, Third International Colloquium on Drops and Bubbles*, edited by T. G. Wang (Am. Inst. Phys., New York, 1989).
32. F. Savart, *Ann. de Chim.* **53**, 337 (1833).
33. W. J. Silliman, Ph.D. thesis, University of Minnesota, 1979 (unpublished).
34. G. Strang and G. J. Fix, *An Analysis of the Finite Element Method* (Prentice–Hall, Englewood Cliffs, NJ, 1973).
35. J. A. Tsamopoulos and R. A. Brown, *J. Fluid Mech.* **127**, 519 (1983).
36. R. A. Walters, *Comput. Fluids* **8**, 265 (1980).
37. T. G. Wang, E. H. Trinh, A. P. Croonquist, and D. D. Elleman, in *Proceedings, Third International Colloquium on Drops and Bubbles*, edited by T. G. Wang (Am. Inst. Phys., New York, 1989).
38. C. E. Weatherburn, *Differential Geometry of Three Dimensions* (Cambridge Univ. Press, Cambridge, UK, 1927).